

## Investigation and Design of a Lightweight Three-Wheeled Vehicle for Optimal Fuel Efficiency

Kristaq Hazizi<sup>1</sup>, Gary Wood<sup>2</sup>, Luka Nakata<sup>3</sup>

<sup>1,2,3</sup> School of Future Transport Engineering, Coventry University, Coventry CV1 2JH, UK.

**ABSTRACT:** The automotive industry is witnessing a paradigm shift towards electric and hydrogen-powered vehicles, underscoring the pressing need for advancements in fuel efficiency for Internal Combustion Engine (ICE) vehicles to sustain their relevance. This paper presents a comprehensive project aimed at investigating and designing a lightweight three-wheeled vehicle for participation in the 2024 Shell Eco-marathon (SEM) prototype class competition, with a targeted fuel efficiency of 1500 km/L. Five primary focus areas were identified: Chassis, Bodywork & Canopy, Powertrain, Gearing & Clutch, and Vehicle Dynamics. Adhering to the Shell Eco-marathon (SEM) rules and regulations, each section underwent meticulous design and investigation processes, leveraging state-of-the-art computer software including Finite Element Analysis (FEA), Computational Fluid Dynamics (CFD), Computer-Aided Design (CAD), and numerical modelling.

This paper presents a comprehensive investigation and design approach towards achieving optimal fuel efficiency in a lightweight three-wheeled vehicle. With the ever-growing concern for environmental sustainability and the increasing demand for fuel-efficient transportation solutions, the development of lightweight vehicles has garnered significant attention. Through rigorous analysis and experimentation, this study explores the key factors influencing fuel efficiency in three-wheeled vehicles, including aerodynamics, vehicle dynamics, powertrain optimisation, and material selection. Leveraging advanced computational tools and experimental validation, novel design strategies are proposed to minimize energy consumption while maintaining structural integrity and safety standards. The research outcome provides valuable insights into the intricate balance between weight reduction, aerodynamic performance, powertrain efficiency, and material utilisation. Moreover, the study investigates the potential impact of emerging technologies, such as electric propulsion systems and lightweight materials, on enhancing the fuel efficiency of three-wheeled vehicles. The interdisciplinary nature of this investigation contributes to the ongoing discourse on sustainable mobility and underscores the potential of lightweight three-wheeled vehicles as a viable solution for achieving optimal fuel efficiency in urban environments.

The resulting designs and concepts were meticulously crafted to align with the predefined objectives of each section. The culmination of these efforts represents a coherent framework poised for manufacturing, with most concept designs deemed ready for implementation in the vehicle assembly phase. Nonetheless, certain components have been identified as necessitating further development to meet the requisite standards. This study not only contributes to the advancement of fuel-efficient ICE vehicles but also lays the groundwork for future research endeavours in automotive engineering and design.

**KEYWORDS:** Fuel efficiency optimisation, Lightweight vehicle design, Three-wheeled vehicle dynamics, Computational analysis, Sustainable transportation, Vehicle aerodynamics, Powertrain efficiency, Material selection for automotive applications.

### INTRODUCTION

The modern world faces a pressing need for sustainable transportation solutions to combat environmental degradation and fossil fuel depletion. In response to this challenge, the automotive industry continually seeks innovative approaches to enhance fuel efficiency and reduce emissions. One promising avenue of exploration lies in the design and development of lightweight vehicles optimized for optimal fuel efficiency.

The study aimed to investigate and design a lightweight three-wheeled vehicle for optimal fuel efficiency, specifically tailored for participation in the Shell Eco-marathon (SEM) prototype class competition. The project was conducted at

Coventry University's School of Future Transport Engineering and involved interdisciplinary collaboration among faculty and students.

### Characteristics of Participants or Description of Materials:

Participants included the Phoenix Racing Eco-Marathon team, consisting of engineering students and researchers. Materials used in the study were state-of-the-art engineering software such as CATIA V5, ANSYS for Finite Element Analysis (FEA), and Computational Fluid Dynamics (CFD) tools for bodywork and aerodynamic analysis. Physical materials included 6063-T6 and 6082 aluminium alloys for

chassis fabrication and Schwalbe Kojak tires for vehicle dynamics testing.

#### **Processes and Methodologies:**

The research employed advanced methodologies including CAD modelling, numerical simulations, and experimental validation. The chassis was designed using aluminium alloys optimized for weight and structural integrity. Aerodynamic performance was analysed using CFD simulations, while rolling resistance and tire efficiency were assessed through a custom-built test rig. Powertrain performance was evaluated through engine modelling and dynamometer testing to optimize fuel efficiency.

#### **Statistical Analysis:**

Descriptive statistics and comparative analyses were conducted to evaluate performance parameters. Statistical power calculations ensured the validity of experimental setups. Variance analyses were used to compare outcomes across different design iterations.

#### **Ethics Approval and Consent:**

This study did not involve human participants, tissue, or animals, and therefore, no ethical approval was required.

#### **Methods/Experimental**

##### **Motivation behind the Study**

The motivation behind this research stems from the urgent necessity to address the environmental impact of transportation while simultaneously meeting the growing demand for mobility. Conventional four-wheeled vehicles, although ubiquitous, often suffer from inefficiencies associated with their weight, aerodynamic drag, and drivetrain complexities. By shifting focus towards lightweight three-wheeled vehicle designs, we aim to capitalize on the inherent advantages of reduced weight and streamlined aerodynamics to achieve significant gains in fuel efficiency.

Furthermore, the versatility and manoeuvrability of three-wheeled vehicles offer unique advantages, particularly in urban environments where space is at a premium. By exploring the potential of lightweight three-wheeled vehicles, we seek to deliver practical solutions that not only enhance fuel economy but also improve urban mobility and reduce congestion.

##### **Objectives of the Research**

The primary objectives of this research are outlined as follows:

**Investigate Existing Lightweight Vehicle Technologies:** Conduct a comprehensive review of existing lightweight vehicle technologies, focusing on materials, design principles, and aerodynamic strategies employed to maximize fuel efficiency.

**Design Optimisation for Lightweight Three-Wheeled Vehicle:** Utilize advanced engineering principles and computer-aided design (CAD) techniques to develop an

innovative lightweight three-wheeled vehicle concept tailored for optimal fuel efficiency.

**Performance Evaluation and Analysis:** Perform detailed simulations and testing to evaluate the performance of the proposed vehicle design in terms of fuel efficiency, aerodynamic efficiency, structural integrity, and overall handling characteristics.

**Comparative Study:** Compare the fuel efficiency and environmental impact of the lightweight three-wheeled vehicle against conventional four-wheeled counterparts under various driving conditions and scenarios.

**Feasibility Assessment:** Conduct a feasibility assessment of the proposed vehicle design, considering factors such as manufacturing feasibility, cost-effectiveness, regulatory compliance, and market acceptance.

By pursuing these objectives, we aim to contribute valuable insights and practical solutions to the ongoing discourse on sustainable transportation, paving the way for the development of next-generation vehicles that are both environmentally responsible and technologically innovative.

##### **Importance of Fuel Efficiency in Transportation:**

The transportation sector is a significant contributor to greenhouse gas emissions and air pollution, which are major concerns for environmental sustainability.

With the global increase in population and urbanization, there has been a corresponding rise in the demand for transportation, leading to greater energy consumption and environmental impact.

Improving fuel efficiency in vehicles is crucial for reducing carbon emissions, mitigating climate change, and promoting energy security.

Governments worldwide are implementing stricter fuel economy standards and regulations to encourage the development and adoption of more fuel-efficient vehicles.

##### **Significance of Lightweight Vehicles:**

Vehicle weight directly impacts fuel consumption and emissions. Heavier vehicles require more energy to accelerate and maintain speed, resulting in higher fuel consumption and emissions.

Lightweighting, the process of reducing a vehicle's weight by advanced materials and design techniques, offers significant benefits in terms of fuel efficiency and environmental sustainability. Lightweight vehicles not only consume less fuel but also exhibit improved handling, acceleration, and braking performance.

Advancements in lightweight materials such as carbon fibre composites, aluminium alloys, and high-strength steel have enabled the development of structurally efficient and lightweight vehicle designs without compromising safety. The automotive industry is increasingly focusing on lightweighting strategies to meet fuel economy targets, comply with regulations, and address consumer demand for more eco-friendly transportation options. By investigating and designing a lightweight three-wheeled vehicle for

## “Investigation and Design of a Lightweight Three-Wheeled Vehicle for Optimal Fuel Efficiency”

optimal fuel efficiency, this research aims to contribute to the ongoing efforts to address these challenges and promote sustainable transportation solutions.

The Shell Eco-marathon (SEM), with its roots tracing back to 1939 and formal inception in 1985, has evolved into a premier platform challenging student team globally. Originating in France, SEM tasks participants with the formidable endeavour of crafting vehicles that not only maximize travel distance but also minimize energy consumption. Beyond the singular focus on fuel efficiency, Shell Eco-marathon (SEM) embodies a broader commitment to environmental stewardship by encouraging innovations that mitigate emissions. This ethos is encapsulated within Shell Eco-marathon SEM's dual categories: Prototype and Urban Concept, which accommodate an array of propulsion systems, including Internal Combustion Engines (ICE), electric motors, and fuel cells.

Among the esteemed contenders in the SEM Prototype category is Coventry University's Phoenix Racing Eco-Marathon team, distinguished for its utilisation of an ICE powered by petrol. The team's inaugural foray into Shell Eco-marathon (SEM) in 2012 marked a journey rife with both triumphs and tribulations. While their maiden vehicle successfully navigated the rigors of technical inspection, it was plagued by challenges stemming from its substantial curb weight and overheating issues, attributed to the design constraints of its thick bodywork. Undeterred by setbacks, the team regrouped in 2021 with a renewed vigour to construct a new vehicle for the 2022 competition. However, persistent engine complications thwarted their aspirations, resulting in their absence from both the 2022 and 2023 editions of (SEM). Embracing the ethos of continuous improvement, the team embarked on a comprehensive redesign initiative for the 2024 competition, driven by insights gleaned from the limitations encountered in previous iterations. A critical revelation emerged from the evaluation of the 2022/2023 model's

chassis, which, while exhibiting adequate stability under static loads, manifested deficiencies in dynamic performance due to its wooden construction, resulting in concerning levels of torsional flex. Addressing this pivotal challenge necessitated a holistic re-evaluation of the vehicle's structural integrity, culminating in a complete overhaul of the chassis design. This strategic pivot not only affords the opportunity to rectify existing shortcomings but also facilitates a holistic reassessment of the vehicle's design, enabling the implementation of enhancements across all pertinent domains.

Central to the endeavour is the development of a lightweight, three-wheeled vehicle configured in a tadpole layout, a configuration characterised by two front wheels and a single rear wheel. This configuration offers inherent advantages in terms of aerodynamic efficiency and manoeuvrability, aligning seamlessly with the overarching objective of optimising fuel efficiency. The investigative scope of this project encompasses five key areas: Chassis, Bodywork and Canopy, Powertrain, Gearing and Clutch, and Vehicle Dynamics. Through meticulous planning and execution, this paper endeavours to document the project's aims, objectives, and the intricacies of the design process within each investigative domain, culminating in comprehensive project conclusions. Crucially, the design methodology adheres rigorously to Shell Eco-Marathon (SEM) competition regulations, ensuring not only compliance but also alignment with SEM's ethos of innovation, sustainability, and environmental responsibility.

### Vehicle Specifications

#### Initial Dimensions

Table 1 presents the initial vehicle dimensions, with particular attention drawn to the wheelbase, which is a manifestation of the design determinations made by the chassis department and shows in Figure 1.

**Table 1 Agreed initial dimensions.**

<b>Wheelbase</b>	1700	mm
<b>Track</b>	800	mm
<b>Width</b>	875	mm
<b>Length</b>	2930	mm
<b>Ground Clearance</b>	150	mm
<b>Ground to Axle</b>	270	mm

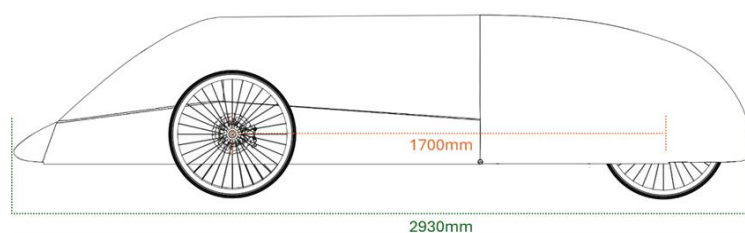


**Figure 1 Vehicle wheelbase and body length diagram.**

**Estimated Weight**

Table 2 provides a comprehensive breakdown of the weight attributed to individual components, culminating in an estimated total vehicle weight of 42.2 kg. Upon inclusion of a 70 kg driver, the projected weight escalates to 112.2 kg.

Weight determination ensued via direct scale measurement for readily accessible parts, alongside estimation derived from precedent designs and online resources for novel components. An additional allowance of 2 kg has been incorporated to accommodate unforeseen components.

**Table 2 Masses of vehicle parts.**

Assembly	Part	Quantity	Mass (kg)			
			Individual	Total	Sum	%
<b>Chassis</b>	Front Tubing	1	3.46	3.46	12.19	28.9%
	Rear Bars	1	2.63	2.63		
	Bulkhead Chassis	1	0.45	0.45		
	Bulkhead Fire Wall	1	1.00	1.00		
	Front Floor	1	3.20	3.20		
	Rear Floor	1	0.97	0.97		
	Front Floor Tabs	14	0.02	0.21		
	Rear Floor Tabs	4	0.02	0.06		
	Firewall Tabs	8	0.03	0.21		
<b>Bodywork &amp; Canopy</b>	Nose cone	1	0.25	0.25	6.90	16.4%
	Front Side Panels	2	0.35	0.70		
	Middle Side Panels	2	0.55	1.10		
	Canopy	1	3.50	3.50		
	Rear cover	1	1.04	1.04		
	Connectors	16	0.02	0.32		
<b>Powertrain</b>	Engine (including clutch)	1	3.33	3.33	7.93	18.8%
	Starter Motor Components	1	0.63	0.63		
	ECU Components	1	1.44	1.44		
	Battery	1	0.49	0.49		
	Fuel System	1	1.12	1.12		
	Wiring	1	0.60	0.60		
	Exhaust	1	0.32	0.32		
<b>Gearing</b>	Input	1	0.20	0.20	2.19	5.2%
	Output	1	0.80	0.80		
	Drive Shaft	2	0.51	1.02		
	Belt	1	0.17	0.17		
<b>Wheels + Uprights</b>	Upright / Stub Shaft	2	0.20	0.41	4.39	10.4%
	Front Wheel	2	1.28	2.56		
	Rear Wheel	1	1.42	1.42		
<b>Steering</b>	Rack / Tyrod	1	0.85	0.85	1.43	3.4%
	Handles + Lever	2	0.14	0.28		
	Pulleys	2	0.15	0.30		
<b>Seats</b>	Back Support	1	0.20	0.20	1.86	4.40%
	Cushion	1	0.04	0.04		
	5-Point-Harness	1	1.62	1.62		
<b>Brakes</b>	Front Brake	2	0.21	0.43	0.64	1.5%
	Rear Brake	1	0.21	0.21		
<b>Pedal</b>	Pedal box	1	1.12	1.12	1.12	2.7%
<b>Other</b>	Horn + Wire	1	0.12	0.12	3.59	8.5%
	Wing Mirror	2	0.05	0.10		

	Speedo	1	0.37	0.37		
	Fire Extinguisher	1	1.00	1.00		
	Non-considered areas (screws, etc.)	1	2.00	2.00		
<b>Driver + Ancillaries (kg)</b>					<b>70</b>	
<b>Kerb Weight (kg)</b>					<b>42.22</b>	
<b>Car + Driver (kg)</b>					<b>112.22</b>	

**LITERATURE REVIEW**

Cars participating in Shell Eco-marathon (SEM) events commonly employ two primary types of chassis designs, namely tubular and monocoque. These chassis configurations serve as the fundamental framework of the vehicle, providing structural integrity and support during the competition. The distinction between the two designs lies in their respective material choices, which dictate their unique characteristics and performance capabilities on the track.

As highlighted by Ahmad et al. (2020) [1], material attributes exert considerable influence on the performance of diverse chassis configurations. Notably, carbon fibre, characterised by its superior strength compared to aluminium, presents distinct mechanical behaviours. While carbon fibre exhibits double the strength of aluminium, it is inherently less flexible due to its susceptibility to fracturing under significant bending loads. Conversely, aluminium offers greater malleability, enabling welding and shaping techniques for stress mitigation. Moreover, the reparability of carbon fibre

components is challenged by the intricate bonding characteristics inherent to the material.

In the investigation conducted by Odi-Owei and Erukainure (2022) [2], the utilisation of aluminium as a constituent material for fabricating a functional Shell Eco-marathon (SEM) chassis was examined. Faced with constraints in material acquisition, the researchers opted to employ a construction method involving the amalgamation of two aluminium angle sections, thereby forming a square tube configuration. It is anticipated that this procedural choice exerted discernible effects on both the mass and structural integrity of the resultant chassis. However, notwithstanding these considerations, the conclusive measurement of the fully assembled chassis yielded a final weight of 15 kilograms. This outcome serves to underscore the enduring promise and viability of aluminium as a material of choice for the construction of Shell Eco-marathon (SEM) vehicles.

Odi-Owei and Erukainure (2022) [2], carried out research focusing on the mechanical attributes of diverse 6063 aluminium alloys. The data presented in

Table 3 demonstrates that 6063-T6 showcased superior tensile and yield strength levels, influencing the preference for this material in chassis production.

**Table 3 Mechanical properties of 6063 Aluminium Alloy [2]**

<b>Alloy &amp; Temper</b>	<b>Diameter or Thickness (mm)</b>	<b>Tensile Strength (MPa)</b>	<b>Yield Strength 0.2% Proof (MPa) min.</b>	<b>Elongation (%) (GL = 50 mm or 5.65√) min.</b>
<b>6063-O</b>	All	130 max	-	16
<b>6063-T1</b>	Up to 12.0	115 min	60	12
	12.0 – 25.00	110 min	55	10
<b>6063-T5</b>	Up to 12.0	150 min	110	8
	12.0 – 25.00	145 min	105	6
<b>6063-T6</b>	Up to 25.00	240 max	215 max	8

In their investigation, Odi-Owei and Erukainure, (2022) [2] undertook an analysis of the dynamic forces and bending stresses exerted upon the chassis during operational conditions. This analytical endeavour encompassed the meticulous calculation of load distribution, elucidating its consequential impact on chassis deflection and shear stress. Leveraging these computations, a Finite Element Analysis (FEA) of the chassis design was meticulously crafted, simulating the imposition of vertical loads. The resultant FEA unveiled a peak stress magnitude of 210 megapascals (MPa) alongside a deflection measure of 65 millimetres (mm). In

addition to internal combustion engines, alternative prototype vehicles for Shell Eco-marathon (SEM) have been explored, including those propelled by hydrogen and electric fuel cells. Aluminium presents a diverse range of possibilities for material selection. A recent investigation conducted by Tsirogianis et al. (2018) [3] involved the construction of a lightweight electrical chassis through the utilization of both aluminium and steel. The overall mass of the chassis amounted to 10.85kg. More specifically, Aluminium 6082-T6 was the aluminium grade employed. This aluminium exhibits a notable Elastic modulus of 72 GPa and a Tensile

strength of 270 MPa, rendering it a favourable option for structural purposes.

Corresponding to the investigation into hydrogen fuel cell vehicles conducted by Tsirogiannis et al. (2018) [4], these endeavours frequently employ aluminium chassis due to their associated advantages, encompassing ease of fabrication, streamlined manufacturing processes, cost efficiency, as well as sufficient structural rigidity and strength. Notably, certain scholarly inquiries advocate for the utilisation of square tubing as opposed to circular tubing, citing simpler cutting and welding methodologies. This consideration significantly influenced the adoption of square tubing within the scope of this application.

Kozák et al. (2022) [5], proposed an alternative chassis structure in their study that deviates from the traditional use of aluminium. The configuration they have devised integrates carbon fibre composite tubes connected by glass fibre nodes produced using 3D printing technology. While the study confirms a reduction in weight, the exact magnitude of this decrease is not specified. Moreover, the analysis fails to include a comparison of expenses between the two distinct designs.

Researchers examined the utilisation of carbon fibre monocoque chassis in the realm of lightweight race cars. Messana et al. (2019) [6] were responsible for conceptualizing and constructing a chassis intended for the prototype division of the Shell Eco-Marathon (SEM) competition. Their publication delves into the intricacies of the production procedure, encompassing the employment of Finite Element Analysis (FEA) to enhance the arrangement and thickness of plies for heightened robustness and rigidity. The conclusive blueprint successfully met their objectives, boasting a mere 11.2 kg in weight. Nevertheless, the investigation concedes the substantial expenses and ecological ramifications associated with carbon fibre technology as prominent impediments.

Rogiest et al. (2011) [7], offer additional backing for the advantages of employing carbon monocoque in the realm of lightweight design. Despite the absence of precise details regarding the chassis weight in their study, the total weight of their vehicle amounted to merely 42.75 kg, positioning it as one of the most lightweight contenders in the competition.

Kah et al. (2010) [8] conducted an examination into the welding characteristics of various aluminium alloys with a specific focus on crack vulnerability. Their research indicates that the chemical composition of the alloy along with the welding procedure itself are important. Particularly noteworthy is the fact that aluminium of the 6XXX series, which contains approximately 1% magnesium silicide, is more inclined to develop cracks, rendering it unsuitable for use as a filler material. To mitigate the occurrence of solidification cracks, it is preferred to utilise filler metals such as 4043 and 5356. Furthermore, in comparison to 6005, 6082 displays a reduced tendency towards liquation cracking.

In the study conducted by Cui et al. (2023) [9], the focus was on the MIG welding process applied to 6063-T6 aluminium. Through their investigation, an optimal welding current of 85A was determined, with currents surpassing 90A yielding joints of diminished strength. An examination of the fracture morphology during tensile testing unveiled that elevated currents induced the formation of larger, yet shallower dimples, a phenomenon directly correlated with the observed decrease in mechanical integrity.

Lucic and Lučić (2023) [10] conducted three static tests, namely shear, overall bending, and lateral bending, to fulfill the FEA simulations for evaluating the chassis rigidity. These examinations offered valuable insights into the fundamental deformation behaviour of the chassis. Nevertheless, incorporating a torsional load test would prove advantageous in attaining a more holistic comprehension of its operational performance in real-world scenarios. Furthermore, given the vehicle's maximum speed limitation of 24 mph, an aerodynamic load analysis is deemed unnecessary as it would not give rise to significant structural apprehensions.

Abo-Serie, Oran and Utcu (2017) [11] conducted an analysis on the foundational aspects of drag force, CD, and airflow distribution, with a focus on strategies for reducing fuel consumption in a theoretical Shell Eco-Marathon (SEM) competition car. The study emphasized the mitigation of "aerodynamic drag, rolling resistance, and mechanical friction between components". Utilising a modified teardrop shape, the researchers introduced the "low drag concept" and examined its performance in a virtual wind tunnel using a "commercial CFD software" to model airflow patterns around the vehicle. By adjusting the underside and the front and rear sections of the teardrop shape based on collected data, the team achieved a decreased CD value of 0.127 compared to the original 0.430. The bodywork design illustrated in the undergraduate thesis holds significance for the subsequent work, as it informs the bodywork development for the Shell Eco-Marathon (SEM) 2024 car.

Fabian et al. (2018) [12] provide insight into the pivotal role of computer-aided design (CAD) software in optimising vehicle shape to minimize fuel consumption, particularly in the realm of structural equation modelling Shell Eco-Marathon (SEM). Focusing on CATIA V5 software, the study delineates its application in shaping objects from a 2D perspective within the context of designing Shell Eco-Marathon (SEM) vehicles. The methodology elucidated underscores CATIA V5's significance in addressing the intricate design complexities inherent in such vehicles, necessitating a tailored approach.

The research outlines a systematic procedure for designing both conventional and Shell Eco-marathon (SEM) vehicles, highlighting the indispensable role of CATIA V5 throughout. Subsequent testing employing computational fluid dynamics (CFD) methods enabled a comparative analysis of drag forces between the two models, revealing discernible variations.

This underscores the meticulous attention required to achieve results closely aligned with real-world parameters. The study's findings hold relevance to the present project, as the methodology employed in shaping vehicle bodywork has been adapted from the procedures outlined for designing conventional and Shell Eco-Marathon (SEM) vehicles.

Santin, (2007) [13] provided an explanation and documentation on the development of the PAC-Car II, emphasizing the importance of aerodynamic drag in determining power demand. The design methodology applied in formulating the bodywork design considered the impact of regulations and various vehicle components. The use of CFD simulations helped enhance the aerodynamic properties of the teardrop-shaped bodywork design. The research findings highlight the suitability of a monocoque carbon fibre chassis for reducing the vehicle's weight and improving structural integrity.

Kozák et al. (2022b) [14] examined the shortcomings of a vehicle previously involved in the Shell Eco-Marathon (SEM) competition, evaluated various aspects of a hypothetical vehicle, and provided blueprints for the 2022 race. An analysis of the regulations and configurations of competitors was carried out to integrate them into a new bodywork design. The study concluded that the bodywork should feature an enhanced teardrop configuration using a composite structure of polystyrene resin reinforced with fibreglass fabric. The authors utilized Computational Fluid Dynamics (CFD) simulations to study the teardrop shape and determined that a teardrop-shaped monocoque carbon fibre chassis is optimal due to its low drag coefficient, material strength, and reduced weight.

Ail Ganesan and Darul Ridzuan (2011) [15] documented the progress and construction of a vehicle intended for future involvement in the Shell Eco-Marathon (SEM) race. During the design prototyping phase, the PAC-Car II and Remmi 7 models were consulted. The refinement of the teardrop configuration in the bodywork was carried out while complying with regulations and design constraints. The incorporation of reinforced glass fiber in the manufacturing process was chosen due to limitations in equipment.

Arpino et al. (2019) [16] utilised the prototype model of an Shell Eco-Marathon (SEM) electric vehicle for conducting aerodynamic assessments, incorporating both numerical and empirical methodologies to analyse the aerodynamic performance and scrutinize the results. The examination vehicle was obtained externally and presented as a complex 3D prototype blueprint. The numerical experiments commenced with 3D CFD simulations, while the empirical techniques involved developing a scaled-down model of 1:18 proportions for testing in the Laboratory of Industrial Measurements wind tunnel. The findings of this study are crucial for interpreting the CFD assessments and the experimental wind tunnel tests, highlighting the importance

of the uncertainty analysis inherent in the experimental procedure.

Pires et al. (2018) [17] conducted an experimental investigation aimed at quantifying the influence of surface roughness on aerodynamic performance within a controlled wind tunnel environment. The study employed the "TUDelft" wind tunnel configuration, characterised by its low-turbulence and low-speed airflow conditions. An upright aerofoil served as the primary test subject, onto which "roughness simulation material" was applied. Concurrently, sensitive microphone apparatuses were strategically positioned in proximity to the aerofoil. Multiple trials were conducted, both with and without the presence of surface roughness on the aerofoil. Analysis of the acquired data revealed a discernible augmentation in the coefficient of drag (CD) ranging between 4% and 15% attributable to surface roughness.

The regulation of airflow surrounding the engine plays a crucial role in the operational capacity of an automobile. The intake of air facilitates advantages such as improved fuel mixture, temperature of the charge, and the potential to influence both the efficiency and emissions of the engine. Research focusing on the design of exhaust systems revealed that an enlargement in the curvature radius resulted in a decrease in exhaust resistance, accompanied by elevated exhaust speeds and diminished emissions [18].

Di Battista, Di Bartolomeo and Cipollone (2018) [19] research has identified a relationship between a decreased intake temperature and a reduced Brake Specific Fuel Consumption (BSFC); BSFC is linked to the quantity of fuel necessary to generate the corresponding engine output. Consequently, a lower BSFC signifies an enhanced engine efficiency by extracting more power from the fuel.

Nevertheless, studies have also indicated that a decline in combustion temperature results in an increased presence of unburned fuel in the exhaust mixture, thereby adversely affecting the cleanliness of the engine. Despite operating more efficiently, the engine emits a higher ratio of CO, CO<sub>2</sub>, Hydrocarbons, and NO<sub>x</sub>.

Li et al. (2010) [20] led to an inquiry into the body of literature concerning combustion temperature, examining the consequences of altering injection timing or airflow rate. A study revealed that modifications in injection angle can result in a beneficial influence on the concentration of CO, while simultaneously having a detrimental effect on the quantity of NO<sub>x</sub> for equivalent adjustments.

The present study proceeds to explore the comparative advantages between an "optimal" and "non-optimal" configuration, with a focus on examining the Brake Mean Effective Pressure (BMEP) and Brake Specific Fuel Consumption (BSFC) metrics. Figure 2 presents the outcomes of this inquiry, demonstrating that through judiciously balancing these variables, a more favourable ratio of fuel-to-power per cylinder pressure can be achieved. This

optimisation continues until reaching a threshold wherein all values converge.

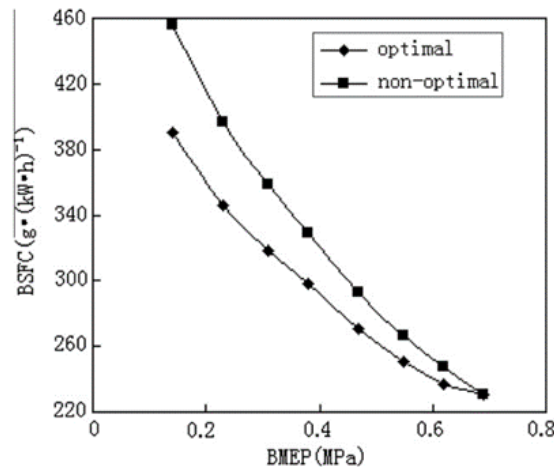


**Figure 2 Relationships of BSFC with BMEP at an engine speed of 1600 rpm with optimal and non-optimal injection timing and ignition timing [20]**

Despite the extensive literature available on the manipulation of the variables, there exists a paucity of direct investigation into fuel conservation through such methodologies. Previous scholarly discourse has predominantly focused on the application of these techniques to ensure the preservation of engine integrity in response to variations in load, fuel injection rates, or vehicle performance. Therefore, this research endeavour aims to provide a tangible demonstration of utilizing these methodologies to facilitate engine maintenance, specifically within the domain of race-oriented fuel-saving strategies. The implications of such findings extend towards broader integration into automotive environments, thereby advancing the discourse surrounding engine optimization and fuel efficiency in high-performance contexts.

Research conducted by Costa and Sodr  (2011) [21] indicates that elevations in compression ratio (CR) are associated with a concurrent rise in exhaust temperature. This thermal augmentation consequently implies a reduction in exhaust air density. In the examination of exhaust data, a noteworthy correlation has been observed concerning exhaust temperature and the compression Ratio (CR). The Compression Ratio, denoting the ratio of maximum cylinder volume at bottom dead centre (BDC) to the minimum volume at top dead centre (TDC), has been found to exert a discernible influence on exhaust temperature. Further studies found that with a higher compression ratio (CR), higher power and torque can be obtained, with a draw back on volumetric efficiency.

Benajes et al. (2019) [22] evaluates passive pre-chamber ignition for high compression ratio spark-ignition engines. This study focuses on improving thermal efficiency and reducing emissions in SI engines. Experimental results show how the passive pre-chamber concept increases efficiency

with good combustion stability and high combustion efficiency in stoichiometric conditions. Nevertheless, maximum lambda attainable with the passive system is similar than that of the conventional spark and much lower compared to the maximum levels reported for the active system.

Ydrefors et al. (2021) [23] have identified, during their research investigation, that the fundamental components influencing rolling resistance can be categorised into two distinct groups: operational conditions and structure. Despite the wide range of influential factors that rolling resistance entails, this section will focus on tire composition, air pressure, as well as slippage and tilt angles. Nonetheless, it is crucial to acknowledge the importance of considering the remaining factors throughout the research.

Goł biewski (2015) [24] conducted a study to examine the influence of tire energy efficiency rating, which is determined by tire construction components like compound and tread, on the fuel consumption of a FIAT Panda. The research revealed a marginal reduction in fuel consumption as the outer diameter increased.

The impact of tyre inflation pressure on rolling resistance in various vehicle categories has been extensively demonstrated. Djordjevic, Jankovic and Jeremic (2009) [25] in their study, conducted empirical assessments on a dry, level asphalt surface utilizing an optical sensor affixed to a passenger vehicle to investigate the relationship between tyre pressure and rolling resistance. The findings revealed a notable 40% decline in rolling resistance at a velocity of 30 km/h following an increase in tyre pressure from 1 to 2 bar.

Research conducted by HOSOBUCHI et al. (2021) [26] delved into the effects of tire pressure on rolling resistance, a crucial consideration in the realm of bicycle performance. Their study, which focused specifically on electric bicycles,

revealed noteworthy findings regarding the relationship between tire pressure and energy expenditure. Specifically, they noted a significant reduction in energy output – to the tune of 17.9% – when tire pressure was increased from 2 to 3 kg/cm<sup>2</sup> (28.4 to 42.7 psi) along a consistent route. These findings underscore the importance of systematically investigating the influence of inflation pressure on rolling resistance, particularly concerning Surface Electric Machines (SEM) tires.

In a recent investigation by Gunev and Iliev (2021) [27], the optimal driving posture was explored to ascertain its implications for both driver comfort and vehicle design optimisation. The study evaluated three distinct positions: reclined, semi-reclined, and seated. Results indicated that the semi-reclined posture, specifically with the head and chest inclined forward, conferred notable advantages. This positioning not only afforded the weight distribution benefits akin to reclined postures but also augmented the driver's perception of vehicle handling through enhanced support to the upper thighs. In prioritising driver well-being during race scenarios, the design considerations encompassed factors such as a sense of control over the vehicle, an unobstructed view of the track, and a seating configuration conducive to prolonged periods of use without inducing undue strain on anatomical regions, notably the neck and chest.

According to Cravero and Marsano (2022) [28] in the most adverse conditions encountered by an open-wheel vehicle, the presence of wheels contributes an additional 40% drag to the total coefficient of drag (Cd). Consequently, it is posited that the Cd of the vehicle, inclusive of attached wheels, would approximate 2.18.

### Material Selection

The examination of existing research literature revealed two primary chassis alternatives for vehicles used in Shell Eco-marathon (SEM) applications: carbon monocoque and aluminium space frame. Given that the current project necessitates a full reconstruction rather than mere alterations

to the current chassis, the decision was made to select the design of an aluminium space frame. As a result, the investigation concentrated on various specifications of aluminium and the ways in which their characteristics are influenced by the processes of forming and manufacturing.

Upon the selection of aluminium for the chassis, Ansys Granta EduPack was utilised to facilitate the process of narrowing down specific material alternatives. The software undertook a comparative analysis of material density and yield strength to achieve a harmonious equilibrium between weight reduction and structural robustness, thereby ensuring that the selected material is optimally engineered for the project. Exhibiting a yield strength of 560 MPa and a density analogous to that of other aluminium alloys, 2196 T8 aluminium presents a commendable amalgamation of properties. Nevertheless, owing to the prevalent copper content in 2XXX series aluminium, it demonstrates deficient weldability and a susceptibility to weld-induced cracking, particularly when inappropriate filler materials are employed. Differing from the characteristics of 6XXX and 7XXX series aluminium alloys, the 5XXX series aluminium exhibits an incapacity for heat treatment, thereby diminishing its ductility and impeding the formation of strengthening second-phase precipitates.

Scholarly investigations suggest that 6XXX series aluminium stands as the predominant material employed in spaceframes for Shell Eco-marathon (SEM) and FS applications. However, an evaluation of the available materials from the supplier revealed the provision of solely three alternatives: 6063 T6, 6082 T4, and 7075 O. Consequently, a comparative analysis was executed to discern the most appropriate selection among these choices. Comprising magnesium and silicon, the 6XXX series aluminium alloys are subjected to heat treatment to enhance their strength, rendering them highly suitable for the construction of lightweight spaceframes. The detailed differentiations in characteristics among the three available extruded aluminium options presented by the supplier are expounded upon in Figure 3.

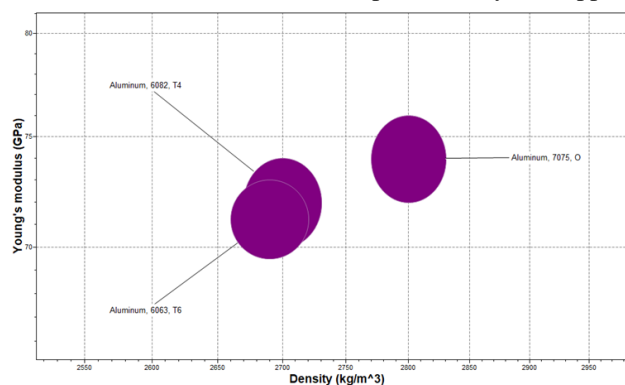


Figure 3 Graph displaying Young's Modulus versus Density of the 3 available aluminium specifications from the supplier.

Table 4 illustrates that 6063 T6 demonstrates the lowest yield strength, accompanied by the lowest density, particularly when compared to 7075. Following consultations with suppliers possessing expertise in FS teams, 6063 T6 surfaced as the most appropriate option. This selection was grounded on its exceptional weldability and formability in contrast to alternative choices. Furthermore, considering that the chassis is not expected to endure high velocities or excessive forces during competitions, unlike FS chassis, the diminished yield strength of 6063 T6 becomes less crucial, thereby averting over-engineering.

To cater to the diverse requirements of the chassis, distinct materials were opted for the front and rear segments. The front necessitated robust, lightweight tubes, leading to the choice of 6063 T6. Conversely, the rear mandated a sturdy bar due to the amplified forces exerted through a single wheel, hence 6082 was chosen as 6063 T6 was unavailable in bar form from the supplier. Fortunately, the aluminium grades exhibit substantial similarity and are capable of being seamlessly welded together, thus the marginal material variance will not impede the manufacturing process.

**Table 4 Mechanical properties of the 3 available material options from the supplier**

Alloy and Temper	Density (kg/m <sup>3</sup> )	Young’s Modulus (GPa)	Yield Strength (MPa)	Tensile Strength (MPa)	Shear Modulus (GPa)	Poisson’s Ratio
<b>6063 T6</b>	2.66e3 – 2.72e3	69.5 – 73	205 – 225	215 – 241	25.3 – 26.6	0.325 – 0.335
<b>6082 T4</b>	2.67e3 – 2.73e3	70 – 74	115 – 134	190 – 222	25.3 – 26.6	0.325 – 0.335
<b>7075 O</b>	2.77e3 – 2.83e3	72 – 76	100 – 120	214 – 236	26 - 28	0.325 – 0.335

The

Table 5 illustrates the various types of 6000 series alloys along with their respective applications. Among these, 6061 alloy is extensively utilised in automotive applications due to

its excellent corrosion and wear resistance, which can be enhanced through specific heat treatments. The 6061 aluminium alloy's medium-to-high strength, combined with its good weldability and machinability, contributes to its versatility.

**Table 5 Detailed material properties for 6061 aluminium alloy.**

Material properties (6061)	Value
<b>Modules of Elasticity</b>	68.9 (GPa)
<b>Fatigue Stress</b>	96.5 (MPa)
<b>Yield Stress</b>	241 (MPa)
<b>Tensile Stress</b>	290 (MPa)
<b>Ultimate Bearing Stress</b>	607 (MPa)
<b>Shear Stress</b>	207 (MPa)
<b>Elongation at Break</b>	12 (%)
<b>Poisson’s Ratio</b>	0.33
<b>Machinability</b>	50 (%)
<b>Thermal Conductivity</b>	167 (W/m-k)
<b>Specific Heat Capacity</b>	0.896 (J/g-°C)

**Tests and Experiment Results**

Following the selection of the material, comprehensive testing was conducted to ascertain its suitability for fabricating the chassis. The primary assessment focused on evaluating the bending characteristics of the tubing to facilitate the fabrication of the roll hoop. A test specimen

comprising 6063 T6 aluminium was procured, accompanied by an appropriate die for the tube bending process to ensure compatibility with the metal. Subsequently, the test specimen was tailored to accommodate both welding and bending evaluations.

## “Investigation and Design of a Lightweight Three-Wheeled Vehicle for Optimal Fuel Efficiency”

The foremost consideration for this material pertained to its bending properties, prompting the initiation of a bending test as the initial step. Utilizing a 180° die set featuring the maximum available centreline radius of 3 inches, the Baileigh tube bender was selected for this purpose. Subsequently, the

tubing strip was positioned within the tube bender apparatus and subjected to a bending operation, achieving a bend angle of 120° to elucidate the material's response to bending forces. Figure 4 illustrates the material's behaviour observed during the conducted test.



**Figure 4 Image of test piece of material in the tube bender.**

Following the completion of the bending test, a welding examination was undertaken to assess the feasibility of fabricating the selected material into a complete chassis structure. Initially, a fish mouth end profile was fashioned on a single piece of material, employing a hole saw with dimensions corresponding to the outer diameter of the tubing. This methodology facilitated enhanced fabrication efficacy by enlarging the contact area, thereby promoting uniform weld formation. Moreover, this step was conducted to emulate the actual chassis manufacturing process, wherein all tubing components would undergo profiling during fabrication. The welding technique employed was Tungsten Inert Gas (TIG) welding, recognized as the preferred method for chassis fabrication. Prior to welding, meticulous surface preparation was undertaken to eliminate any oxide layers, ensuring the creation of pristine weld joints. Figure 5 illustrates the weldability of the material, portraying a uniform weld formation with minimal heat dispersion observed across both the material and the weld joint. Given the material's favourable weldability demonstrated during testing, coupled with the successful outcome of the bending evaluation, it was concluded that the chosen material possessed requisite characteristics for chassis manufacturing. Consequently, the chassis design phase commenced accordingly.



**Figure 5 Image showing the welding test.**

## “Investigation and Design of a Lightweight Three-Wheeled Vehicle for Optimal Fuel Efficiency”

The experimental wind tunnel was dedicated to examining the 3D bodywork model, serving as a physical experimental trial. The vehicle was positioned on the supporting strut, while the

testing platform was adjusted to 150 mm from the bodywork to align with the distance specified in the CFD simulation, illustrated in Figure 6.



**Figure 6** The ground clearance setup during the wind tunnel experiment.

Strings were affixed to the surface of the model to facilitate visualization of flow characteristics, as depicted in Figure 7. Adhesive tape was employed to seal the interstices between individual sections of the bodywork, thereby mitigating potential inaccuracies. The wind tunnel experimentation was executed across a range of wind velocities, repeated iteratively to ensure the precision of resultant data. A reverse

orientation test was undertaken on the bodywork to ascertain the consistency of values relative to the teardrop configuration. Supplementary assessments were performed, including trials at varying yaw angles, employing identical wind velocities as the tests. After data acquisition, analysis was conducted utilising Excel software.



**Figure 7** : The 3D printed bodywork with strings attached in the wind tunnel experiment.

### Tyre Test Rig

Figure 8 illustrates the tyre testing apparatus, which emphasizes simplicity and versatility for potential future test conditions. The main elements comprise of cold-pressed steel tubes serving as the structural framework, 3D-printed joint components made of Polylactic Acid (PLA) and Onyx

filament and a central Medium-Density Fibreboard (MDF), (12mm) enclosure.

The current design configuration enables fundamental steering functionality using elementary front uprights. Nevertheless, additional development is required to incorporate an efficient steering lock mechanism to facilitate more extensive testing.



**Figure 8** Tyre test rig.

Table 6 provides the detailed specifications of the test rig. The design emulates the concept vehicle’s wheelbase and maintains a comparable weight distribution to ensure realistic testing conditions. The track width is currently 100 mm

**Table 6 Tyre test rig specification.**

Property	Value	Unit
Mass	14	kg
Mass Distribution	57.1	%
Wheelbase	1700	mm
Track	700	mm
Estimated Cd	1.05	-
Approximate Frontal Area	0.178	m <sup>2</sup>

narrower; however, it can be readily adjusted with longer axles should future tests incorporate steering mechanisms. The drag coefficient of the rig, estimated at 1.05, is based on the cuboid geometry of the structure [29].

**Test Methodology**

The specified testing region presented an initial decline in elevation. The initial placement of the testing apparatus,

measured from the back wheel, was defined at 6 meters prior to the point where the surface became level. This arrangement is illustrated in the free-body diagram Figure 9.

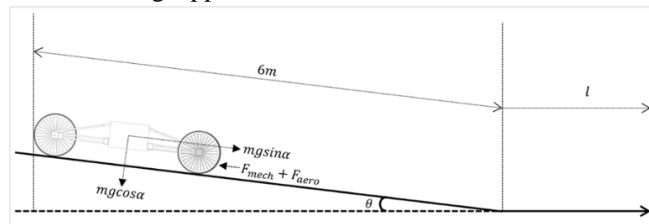


**Figure 9 Free-body diagram for the rolling resistance coast down test.**

The data obtained is displayed in

Table 7. The experimental protocol involved initiating the motion of the apparatus from a stationary position on an inclined plane, without the application of any external force

(i.e., no pushing or pulling). Subsequently, the apparatus was allowed to descend the incline until it reached a complete stop (final velocity of 0 m/s). The total displacement covered by the apparatus and the corresponding time duration were carefully documented.

**Table 7 Slope gradient of test area.**

Distance (m)	Gradient (°)
1	5
2	4
3	3
4	3
5	2
6	3
=>7	0

**Inflation Pressure Results**

As anticipated from existing literature [30]; [31] a linear decrease in the rolling resistance coefficient ( $C_{rr}$ ) was observed with increasing inflation pressure. This phenomenon can be attributed to several factors, including a reduction in the contact patch area as the tire assumes a more circular shape, as well as a decrease in hysteresis.

There exists a noticeable disparity in the absolute values of the rolling resistance coefficient ( $C_{rr}$ ) between the experimental and online datasets as shown in Figure 10. Particularly noteworthy is the presence of a pressure offset.

For instance, the experimental  $C_{rr}$  at 5 bar pressure was only 0.00003 lower than the online  $C_{rr}$  at 4 bar pressure. A similar pattern persists across the 5.5 and 6 bar pressure levels, with a 2.7% variation observed. The most plausible explanation for this variation is the difference in load conditions. The experimental setup applied significantly lower loads (averaging 4.67 kg per tire) compared to the 42.5 kg load reported in the online data, which likely led to an increased  $C_{rr}$ , as elaborated in the subsequent section. Furthermore, the online dataset examined the 28-inch variant of Schwalbe

Kojak tires, which may have contributed to the observed disparities.

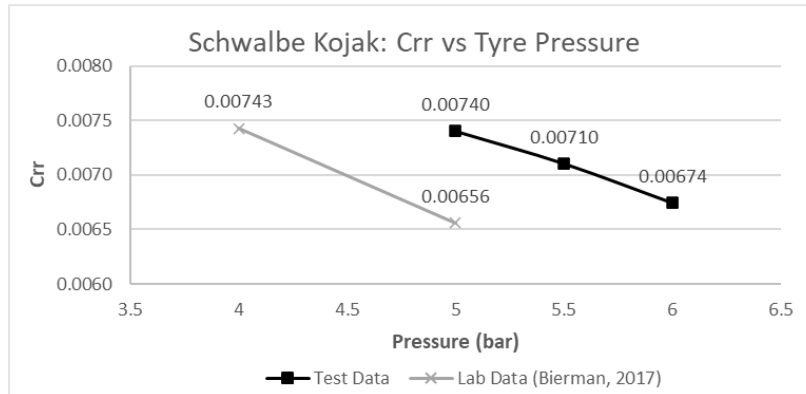


Figure 10 Schwalbe Kojak rolling resistance due to inflation pressure test results.

**Mass Results**

With reference to the findings depicted in Figure 11, a reevaluation of the rolling resistance at 6 bar pressure, with no additional load (total weight 14 kg), was conducted. This retesting revealed a notable 10.6% reduction in C<sub>rr</sub> compared to the initial pressure test data. External factors, such as variations in surface wetness, previously documented to elevate rolling resistance, are likely contributors to this

observed deviation. Specifically, it is noted that there was less rainfall preceding the mass testing in comparison to the initial pressure test, thus influencing the experimental outcomes. Furthermore, the experiment documented a non-linear decrease in C<sub>rr</sub> with increasing load, culminating in a maximum load of 29 kg, attributable to the constraints of the test rig.

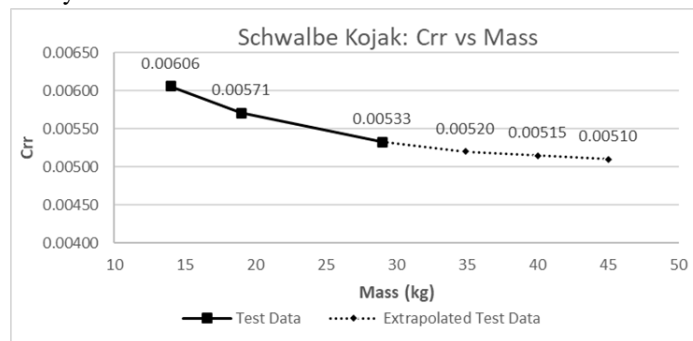


Figure 11 Schwalbe Kojak rolling resistance due to mass test results.

**Initial and Final CAD Wireframe Design Chassis**

The original design was formulated utilising CATIA V5, involving the creation of a wireframe model for the chassis. To attain a balance between lightweight construction and

minimized drag, the chassis and bodywork were developed in tandem. Previous vehicle measurements, especially those influencing driver ergonomics, were referenced to pinpoint sections suitable for material reduction.

Table 8 presents a comprehensive summary of critical measurements transferred from the legacy vehicle, serving as

foundational data for design reference in the context of this research study.

Table 8 Key measurements taken from the old vehicle.

Old Vehicle Measurements	Distance (mm)
Height of bulkhead	650
Width of driver’s compartment	480
Length of driver’s compartment	1700

The primary consideration addressed with the bodywork division was to establish a condition where the front nose of the chassis would be positioned lower than the front

suspension uprights. This adjustment aimed to enhance the driver's field of vision, consequently expanding the potential canopy coverage. Emphasis on driver ergonomics was

“Investigation and Design of a Lightweight Three-Wheeled Vehicle for Optimal Fuel Efficiency”

evident right from the beginning. The inception of the chassis design involved the focal point of the driver compartment, incorporating the driver's anthropometric measurements to

ensure a satisfactory semi-recumbent posture, as illustrated in Figure 12.

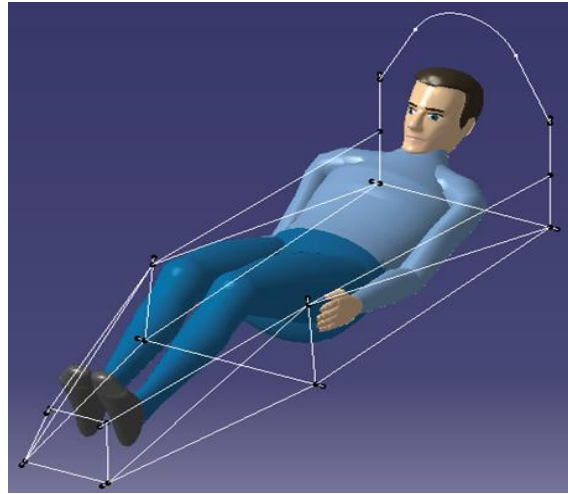


Figure 12 Displaying the driver CAD model lying in the initial wireframe model.

To enhance aerodynamic performance, the collaboration with the bodywork department resulted in the implementation of angled and inward-sloping tubes for the nose and suspension. This design feature enables a more precise alignment of the bodywork with the chassis and promotes the creation of a larger curved frontal area.

Certain tube elements were specifically crafted to extend slightly from the main structure. This strategy streamlines the manufacturing process by providing a greater welding surface, while simultaneously boosting the overall structural integrity through an expanded contact area for welds. The protruding tubes are visually represented by the red nodes in Figure 13.

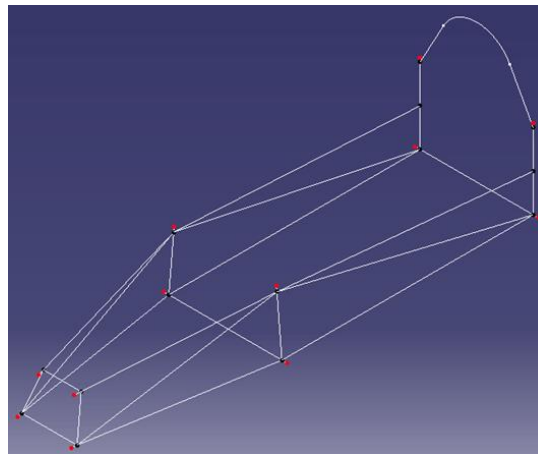


Figure 13 CAD model of the initial wireframe, displaying the tubing that will have 20mm extra material protruding.

Table 9 presents the data regarding the dimensions of the operator's cab in the recently developed chassis.

Table 9 Chassis measurements for driver’s compartment taken from CAD design.

Description	Length (mm)
Lower Front Nose	220
Lower Front Nose to Lower Middle Underbody	700
Total length of Driver’s Compartment	1700
Width of main part of Driver’s Compartment	450
Height of Roll Hoop	550

## “Investigation and Design of a Lightweight Three-Wheeled Vehicle for Optimal Fuel Efficiency”

Following the finalisation of the tubular design, meticulous attention was directed towards the holistic development of the chassis. This involved the formulation of a unified floor design spanning all sections of the chassis, alongside the integration of floor tabs facilitating seamless bolting of the

floor to the chassis assembly. Figure 14 illustrates the conclusive chassis design, featuring the comprehensive incorporation of all pertinent components within the design framework.



**Figure 14 Complete Chassis CAD Design with driver model.**

The conclusive measurements were acquired from the CAD model, facilitating the determination of chassis dimensions after the integration of all components and the profiling of tubing elements. Moreover, through the assignment of

materials to the respective parts within the CAD model, an assessment of the overall chassis mass was compiled and documented in

Table 10.

**Table 10 Complete Chassis Measurements taken from CAD design.**

Description	Measurement
Distance between tubing at firewall	431 (mm)
Distance between firewall and the rear of the chassis	695 (mm)
Distance from the front to rear of the chassis	2407 (mm)
Mass Estimate of Complete Chassis	12.19 (kg)

The primary phase in refining the chassis design necessitates prioritising the conclusion of the fabrication process. The tangible chassis resulting from this phase will serve as the foundation for real-world testing, thereby facilitating a definitive appraisal of the design's appropriateness for its designated application. A pivotal component of this assessment will involve ascertaining the dynamic stiffness of the chassis, thereby ensuring that operational efficiency remains uncompromised. Concurrently, an ergonomic

examination of the driver compartment merits attention to explore the viability of widening it to accommodate a broader spectrum of driver body sizes.

### **Bodywork and canopy design development**

The initial prototype was created utilising Blender software without considering any prototype chassis design and dimensions, as the chassis had not been developed at that point. Numerous iterations were produced, enhancing the shape significantly, as depicted in the Figure 15.

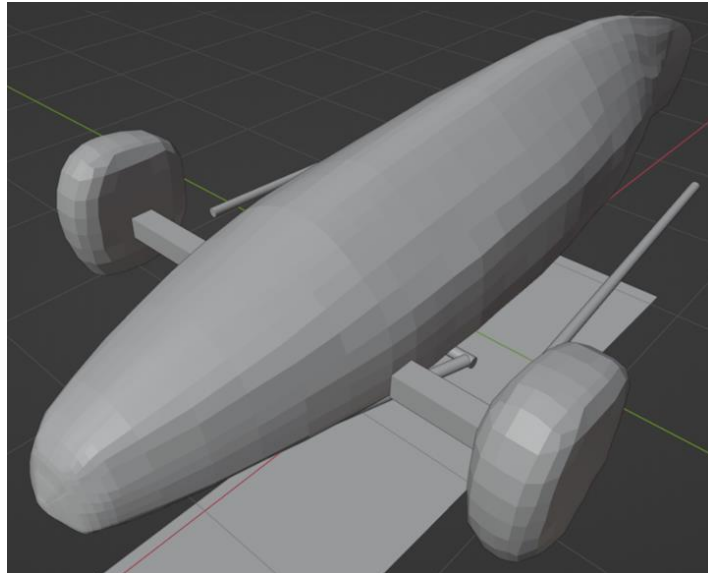


**Figure 15 Blender model of the latest prototype bodywork.**

Blender, recognised as a prominent design software, presents limitations in its capacity to directly manipulate files in CAD format, impeding functionalities such as file opening, sharing, exporting, or conversion within this specialized format. However, it does offer the capability to export designs in STL format, facilitating compatibility with CAD software systems. Consequently, for the design of the bodywork and canopy components, CATIA V5, a prominent CAD software platform, was employed. This strategic decision underscores the pragmatic approach of integrating diverse software tools tailored to specific design requirements within the broader design framework.

The process of crafting the new bodywork design involved the creation of multiple wire sections spanning the car's length, each derived by duplicating the chassis outline and subsequently interconnecting them to establish panels.

However, limitations in proficiency with the generative shape design feature within CATIA V5 resulted in a suboptimal surface finish and the absence of essential components such as a nosecone and rear-end cover. To address the surface irregularities, the potential refinement approach of augmenting the number of wire sections to achieve a smoother texture was proposed. Subsequent design iterations were executed using the freestyle method due to deficiencies in navigating the generative shape design paradigm. Notably, the generation of 2D top, front, and side views of the chassis was instrumental in guiding the bodywork design process. In the final iteration, illustrated in Figure 16, noticeable improvements in the overall surface quality were observed compared to previous iterations, coupled with the successful incorporation of a nosecone into the frontal design.

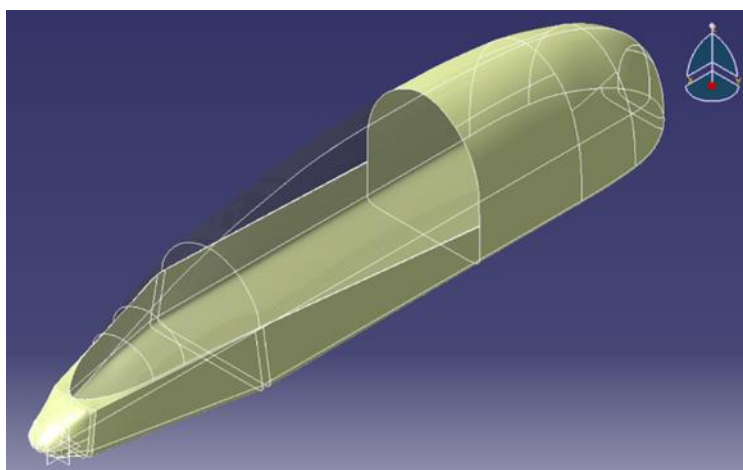


**Figure 16 CATIA model of the final prototype bodywork.**

### **Powertrain Design and Development**

From the aim and objectives of the department, the decision was made to develop an engine model for this project.

Utilising GT-SUITE software, specifically GT-Power, the engine model was designed and tested. Prior to commencing

“Investigation and Design of a Lightweight Three-Wheeled Vehicle for Optimal Fuel Efficiency”

the construction of the model, thorough research was conducted due to the absence of an existing engine model to ensure precise initial observations. The chosen engine for this

project was the Honda GX35, depicted in Figure 17, originally intended for lawnmower use and equipped with a carburettor for fuel flow control.



Figure 17 Honda GX35 Side view.

An intake and fuel injector were later added to modify the engine, along with a custom exhaust featuring a lambda sensor, while other components remained unaltered. Measurements from seized engines were taken to create the model, using Vernier Callipers for all relevant data. For more complex details, an optical measuring device leveraging light and shadows with a geometric axis was utilised to record measurements up to 0.04µm. The initial model was

developed based on the gathered data to facilitate further validation and collection of flow values that were unattainable in-house. Supplementary data from Table 11 was incorporated to fill in missing data points, enabling simulation of the engine model after slight adjustments to the data collection process. After the model simulation, engine development was undertaken to explore the performance capabilities of the engine unit.

Table 11 Flow Data.

Intake L/D	Cd	Exhaust L/D	Cd
0	0	0	0
0.032258	0.070618	0.035714	0.077398
0.064516	0.141237	0.071429	0.174145
0.096774	0.200991	0.107143	0.251543
0.129032	0.244448	0.142857	0.303141
0.16129	0.260745	0.178571	0.32894
0.193548	0.282474	0.214286	0.354739
0.225806	0.293338	0.25	0.367639
0.258065	0.304202	0.285714	0.374089
0.290323	0.309635	0.321429	0.380539
0.322581	0.309635	0.348571	0.386988

The primary focus was aligning the engine model's data with the manufacturer's specifications to ensure logical outcomes. This progressive development approach involved dissecting specific areas to comprehend the underlying characteristics, namely the Air/Fuel ratio targeting leaner combustion compared to the standard 14.7:1 ratio in conventional petrol engines, adjusting the Fuel Injection rate below the standard 6 g/s without causing damage to the engine, and fine-tuning the burn duration to accurately reflect the engine's behaviour. Upon the completion of the initial model of the engine, simulation testing was conducted to compare it with the data provided by the manufacturer. The data furnished by the manufacturer, alongside secondary research, included details

regarding the carburettor and potential enhancements to the engine. Consequently, the primary objective was to align the trends of the data with this information. Subsequent validation would ideally involve comparison with physical engine testing. However, this proved unfeasible due to the complexities associated with engine operation. The results of the initial simulation are depicted in Figure 18, showing a correlation with the supplied data. Notably, both Torque and Power exhibited a decrease in comparison to the manufacturer data, a result that was anticipated given the distinct design aspects of the engine. The Honda data, for instance, was derived using a carburettor and other unique

features pertinent to its original application, including a choke mechanism.

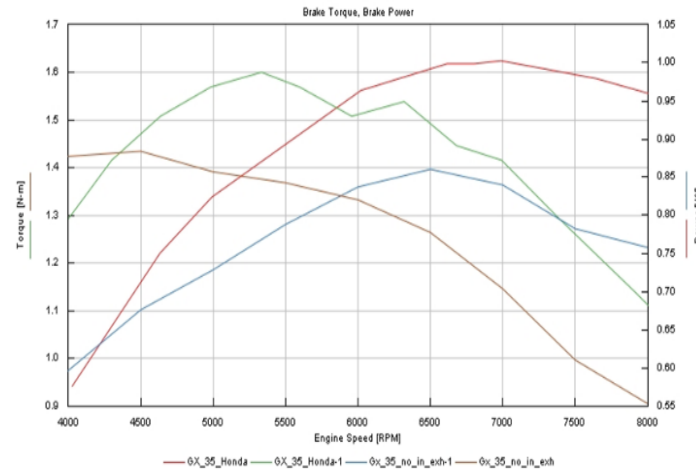


Figure 18 Brake Torque, Brake Power comparisons to supplier data.

At first, the exhaust system was developed based on the uncomplicated geometry of the component. Subsequently, it

Underwent processing by the software to transform it into a two-dimensional representation for incorporation into the overall engine design, as illustrated in Figure 19.

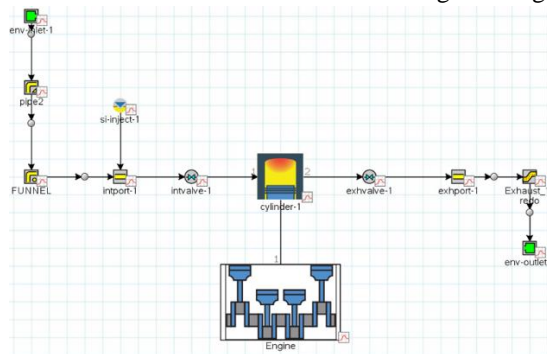


Figure 19 Engine Model with intake and exhaust.

Upon the integration of intake and exhaust components into the system, a subsequent round of simulations was conducted. The findings revealed a notable augmentation in both torque and power output. This outcome was anticipated, attributed to the heightened influx of air into the intake port facilitated by increased velocities and greater mass flow. While this system yields favourable results in terms of engine performance enhancements, the primary objective of its design remains centered on fuel economy. Hence, the parameters of interest primarily revolve around Brake-Specific Fuel Consumption (BSFC) and injected mass flow rate.

Figure 20 illustrates a comprehensive analysis of the principal attributes under investigation. Of particular interest is the

observation that despite a decrease in BSFC, indicative of improved power extraction efficiency from the fuel consumed, this heightened performance necessitated a 10.15% increase in fuel mass input per unit time during testing. While initially appearing advantageous, this trend imposes constraints on the permissible duration of the engine's power cycle. Nevertheless, it does afford the possibility of leveraging greater torque for vehicular propulsion, potentially influencing considerations such as gear ratio and the vehicle's overall mass. Nonetheless, further experimental inquiry is warranted to validate these preliminary findings.

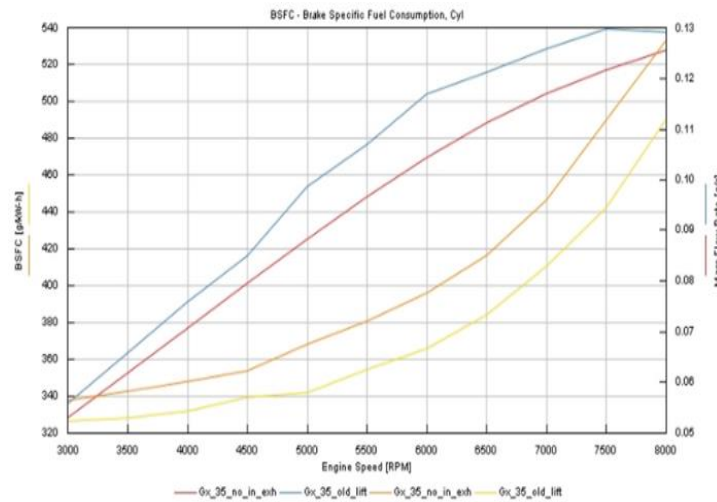


Figure 20 BSFC comparison between the basic engine and the intakes and exhaust model.

The baseline data enabled the initial gathering of timing data, which was essential for conducting the prediction of fuel injector injection flow rates. A scale factor of 93.75 was derived and utilised for this purpose, stemming from the necessity to adjust the race distance from 16 km to the target distance of 1500 km. During the subsequent phase of the

study, foundational data was collected and compared with a decrease in intake length, thus imitating the transition from an active intake system to a passive one, given that the shorter intake is located within the engine bay in contrast to the longer active system. The results illustrated in

of the engine. However, this modification is also linked to a reduction in the engine's ability to produce torque.

Table 12 offer support for the idea that a truncated intake system has the potential to prolong the operational duration

Table 12 Time on and Torque comparison between with initial intake and proposed intake.

RPM	Time On (s)			Torque (Nm)		
	Baseline	Reduced Intake	Δ%	Baseline	Reduced Intake	Δ%
6000	65.079	69.986	7.54	2.010	1.827	-9.10
5500	74.172	77.193	4.07	1.938	1.842	-4.95
5000	81.379	86.355	6.11	1.992	1.840	-7.63
4500	94.149	96.777	2.79	1.917	1.857	-3.13
4000	105.093	109.480	4.17	1.970	1.869	-5.13
3500	122.337	127.474	4.20	1.939	1.839	-5.16
3000	142.793	147.150	3.05	1.944	1.872	-3.70

Additional examination was carried out on the compression ratio, beginning with a baseline of 8:2 and progressively increasing the ratio to 13:1 to monitor its effects on efficiency, power, torque, and longevity. Evaluation of the

compression ratio indicated that a higher ratio resulted in an extended operational time for the engine, as evidenced by the reduced mass flow through the injector, as illustrated in Figure 21.

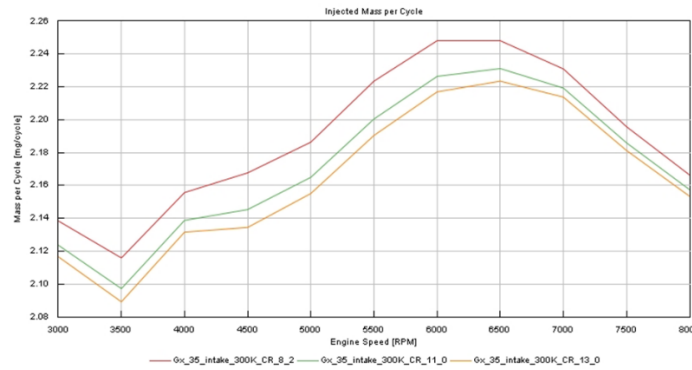


Figure 21 ACT (Air Charge Temperature) impact on inject mass per cycle.

The increase in torque coinciding with variations in Compression Ratio (CR) can be attributed to the amplification in cylinder volume. Notably, CR exerts a substantial influence on the broader functioning of the engine, primarily by elevating the pressure within the combustion chamber, thereby predisposing the piston to detonation. An examination of the influence of heightened CR on Brake Mean Effective Pressure (BMEP) also affords insights into cylinder temperatures.

Figure 22 illustrates data indicating elevated pressure levels within the cylinders corresponding to increased Compression Ratio (CR) values. However, it was observed that the temperature of the cylinders decreased with the rise in CR. Consequently, a comparative examination is warranted to investigate the ramifications on the engine of operating under "worst-case conditions," specifically exploring the effects of higher Air Charge Temperature (ACT) and a larger CR.

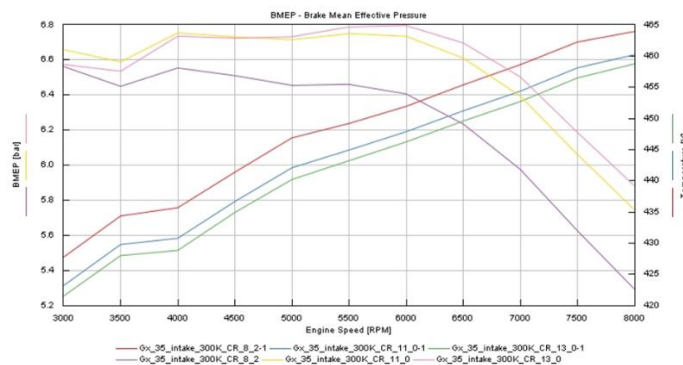


Figure 22 CR impact on BMEP and Cylinder Temperature.

As depicted in

Table 13, operating the engine within the upper temperature threshold while increasing the Compression Ratio (CR) yields the longest duration for the engine's active cycle. These characteristic merits thorough evaluation through comprehensive system dynamometer testing. While the data exhibits positive indications regarding engine uptime, it lacks insights into emissions impact, engine lifecycle, and the effects of cyclic operation and temperature variations.

Additionally, torque values are subject to influence based on the Air Charge Temperature (ACT) and the chosen CR. In terms of optimization, while CR remains a fixed physical parameter post-adjustment, ACT remains variable, posing a challenge for simulation accuracy in comparison to real-world scenarios. Consequently, this dataset should inform predictions for physical testing and facilitate the formulation of Engine Control Unit (ECU) maps for relevant sensors. Moreover, it should guide future optimisation endeavours aimed at enhancing fuel efficiency.

Table 13 CR and ACT comparisons to Time on amount.

RPM	Time on (s)			
	BASELINE	380K-8.2CR	380K-11CR	380K-13CR
6000	69.986	75.595	76.327	76.650
5500	77.193	83.613	84.462	84.823
5000	86.355	93.735	94.769	95.277
4500	96.777	104.535	105.503	105.974

<b>4000</b>	109.481	118.426	119.381	119.716
<b>3500</b>	127.474	137.338	138.499	139.090
<b>3000</b>	147.150	158.223	159.323	159.765

**Gearing and Clutch Analytic Calculation and Design**

Due to the vehicle's incomplete assembly, initial assumptions will be required, depending on relevant factors such as driver weight, engine power output, rolling resistance, and efficiency goals. In this scenario, it is presumed that the mean weight of the operator amounts to approximately 70 kg. Employing an average weight introduces significant partiality into the computation, thereby enhancing the precision of the

outcome. Given that the operator's weight is directly proportional to the torque, it becomes crucial to incorporate a safety margin of 10% for the weight estimation. With that being stated, the effective weight of the project operator falls below the safety margin by approximately 2 kg, rendering it a justifiable assumption. Weight calculation is provided as follows.

$$weight = mass (m) * acceleration of gravity (g) = 70 * 9.8 = 754.6 N \tag{Equation 1}$$

Assume that total weight of the vehicle is 112 kg, calculating the weight as follow.

$$weight = mass (m) * acceleration of gravity (g) = 112 * 9.8 = 1097 N \tag{Equation 2}$$

As a result of the engine's specifications, a peak power of 1 kW and 8000 rpm is delivered. The conversion of both power and resolution into meaningful data is necessary, whereby torque and velocity are obtained. It is of utmost importance to ascertain the precise maximum torque and velocity that the engine can produce, to determine the fulfilment of torque requirements. An appropriate approach may be employed to amplify the torque applied to the rear wheel, thereby achieving the desired level of performance. To determine the torque required at the wheels, it is essential to consider the

efficiency of the wheels and calculate the force necessary to propel the vehicle at its maximum speed. Radius of the Michelin 44-406 has been given in the Shell Eco-marathon (SEM) book, which regulated to be 480 mm maximum of outer diameter. The wheel efficiency has been stated in the objective to be 85%. Velocity (v) = 25 mph = 11.176 m/s, air density (ρ) = 1.225 kg/m<sup>3</sup>, rolling resistance coefficient (f<sub>rr</sub>) = 0.00606, frontal area (A) = 0.15 m<sup>2</sup>, aerodynamic drag coefficient (C<sub>D</sub>) = 0.3. The aerodynamic drag force (F<sub>D</sub>) is calculated as follows.

$$F_D = \frac{1}{2} * \rho * c_D * A * v^2 = 0.5 * 1.225 * 0.3 * 0.15 * (11.176)^2 = 3.4 N \tag{Equation 3}$$

Based on the general characteristics of racetracks and motorsport facilities, it can be inferred that the track surface of Circuit Paul Armagnac is likely constructed from asphalt. Asphalt is the predominant material used for racetracks due to its smoothness, durability, and capacity to provide high levels of grip for racing vehicles. These properties make asphalt the preferred choice for ensuring optimal performance

and safety in motorsport applications. To initiate the motion of a vehicle, it is necessary to overcome the tractive resistance (F<sub>R</sub>), which includes components such as rolling resistance, gradient resistance (climbing), acceleration resistance, and aerodynamic drag. When considering clutch and gearing systems, it is particularly crucial to account for rolling resistance force (F<sub>rr</sub>) is calculated as follows.

$$F_{rr} = f_{rr} * m * g = 0.00606 * 112 * 9.81 = 6.65 N \tag{Equation 4}$$

Total tractive force is needed to find the gear ratio.

$$Tractive Force = Rolling Resistance Force + Aerodynamic Drag Force \tag{Equation 5}$$

$$F_t = F_{rr} + F_D = 6.65 + 3.4 = 10.05 N \tag{Equation 6}$$

Maximum available torque of 1 kw engine is given to be 2.01 Nm. Required torque at the wheel is calculated as follows.

$$Required Torque = Tractive Force \times Wheel Radius = 10.05 * 0.24 = 2.41 Nm \tag{Equation 7}$$

$$Actual Torque Needed = 2.98 * (1 + 0.15) = 3.46 N \tag{Equation 8}$$

To determine the gear ratio of the system, the torque needed at the wheels is divided by the available torque from the engine.

$$gear ratio = \frac{torque at wheels}{max torque available} = \frac{3.46}{2.01} = 1.72 \tag{Equation 9}$$

To achieve a specific acceleration on flat ground, as dictated by the given parameters, the gear ratio must be adjusted to a 1:2 ratio. This implies that the rear wheel pulley diameter is twice the size of the engine drive pulley diameter.

The consideration of slope condition as an external factor is crucial, given its significant influence on the initial difficulty encountered when commencing vehicle movement. As evidenced by a study in the 2016 Shell Eco-marathon (SEM), a 3° incline marked the beginning of the race, posing challenges for all teams in achieving smooth vehicle

propulsion due to oversight of this slope factor. Even the Paul Armagnac, known for its somewhat unpredictable performance, was affected. It is advisable to determine the minimum torque necessary for initiating movement on such inclines. By leveraging the average engine torque of 1.5 Nm and a wheel efficiency of 0.85, one can compute the essential torque for starting the vehicle and identify the requisite gear ratio for ascending a 3° hill while accommodating a total car weight of 112 kg. The total force can be calculated as follows.

$$\text{Total Force} = \text{Force due to Slope} + \text{Force due to Rolling Resistance} \quad \text{Equation 10}$$

$$\text{Force Slope} = \text{Weight of the Car} * \text{Gravitational Acceleration} * \sin(\text{Incline Angle}) \quad \text{Equation 11}$$

$$\text{Force Slope} = 112 \text{ (kg)} * 9.8 \left(\frac{\text{m}}{\text{s}^2}\right) * \sin(3^\circ) = 57 \text{ N} \quad \text{Equation 12}$$

$$\text{Force Rolling Resistance} = \text{Weight of the Car} * \text{Gravitational Acceleration} * \cos(\text{Incline Angle}) \quad \text{Equation 13}$$

$$\text{Force Rolling Resistance} = 112 \text{ (kg)} * 9.8 \left(\frac{\text{m}}{\text{s}^2}\right) * \cos(3^\circ) * 0.006 = 5.3 \text{ N} \quad \text{Equation 14}$$

$$\text{Total Force} = 57 + 5.3 + 6.3 = 68.6 \text{ N} \quad \text{Equation 15}$$

$$\text{Torque at Wheels} = \frac{68.6 \text{ (N)} * 0.24 \text{ (m)}}{0.85} = 19.36 \text{ Nm} \quad \text{Equation 16}$$

$$\text{Gear Ratio} = \frac{19.36 \left(\frac{\text{N}}{\text{m}}\right)}{1.5 \left(\frac{\text{N}}{\text{m}}\right)} = 12.9 = 13 \quad \text{Equation 17}$$

In conclusion, the vehicle weighing 112 kg necessitates a minimum gear ratio of 1:2 to counteract the friction on a level surface, while a maximum gear ratio of 1:13 is crucial to surmount a 3° incline. It is essential to account for external variables like bearing friction and part friction when determining the optimal gear ratio to strike a harmonious balance between the weight of the vehicle and other mechanical systems. Therefore, it is advisable to adopt an intermediate ratio that lies between the extremes to optimise performance.

### Vehicle Dynamics

#### Centre of Gravity & Mass Distribution

The methodology employed to determine the Centre of Gravity (CoG) location is outlined as follows:

- Utilising Computer-Aided Design (CAD), the CoG for each group was determined by measuring the

horizontal (x) and vertical (z) distances relative to both the front axle and the ground plane, respectively. The outcomes are illustrated in Figure 23.

- The moments were computed by multiplying the mass of each group by its corresponding moment arm (x and z distances) to ascertain the group's x and z moments.
- The x and z moments for the entire vehicle were computed by summing all individual group moments. Subsequently, dividing these aggregated moments by the total mass of the vehicle yielded the comprehensive CoG location.

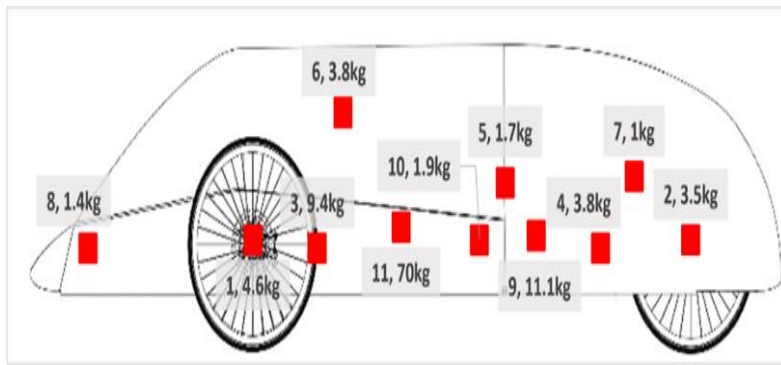


Figure 23 CoG locations for grouped parts.

Figure 24 provides a visual representation of the estimated Centre of Gravity (CoG) positions for scenarios with and without a driver. The corresponding x and z coordinates are

detailed in Table 14. It is imperative to acknowledge that the y-coordinate was assumed to be evenly distributed due to uncertainties surrounding the final placement of components.

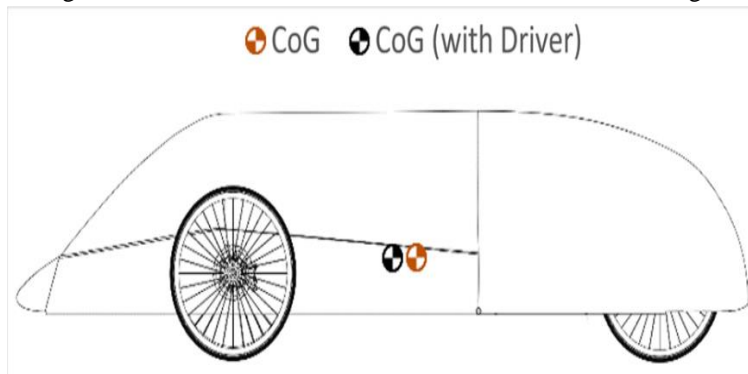


Figure 24 CoG location with and without driver.

Table 14 CoG location coordinates.

	x (mm)	Assumed y (mm)	z (mm)
CoG (With Driver)	634	425	301

Moving forward, the analysis will concentrate exclusively on the inclusion of the driver in determining the vehicle's Centre of Gravity (CoG). The information presented in

depicted in Figure 24. This phenomenon can be attributed to the substantial weight of the driver, who serves as the heaviest "component," with their legs predominantly positioned over the front axle.

Table 15 elucidates a front-heavy weight distribution. While the vehicle exhibits a front bias in isolation, the CoG shifts further towards the front when the driver is considered, as

Table 15 Distribution (%), mass distribution and vertical load on front and rear axle.

	Front Axles	Rear Axle
Weight Distribution (%)	62.7%	37.3%
Mass (kg)	70.38	41.85
Vertical Force (N)	690.4	410.5

**Tyre Specifications**

The Schwalbe Kojak tread-less slick tires, measuring 20 inches (35-406), were obtained already mounted on a wheel and hub unit as part of the Shell Eco-Marathon (SEM) vehicle design project conducted last year. Although specific

information on the tire's composition was not easily accessible, an examination of Figure 25 indicates a bias-ply structure with a protective belt made of 'RaceGuard' (consisting of double-layer nylon).



Figure 25 Schwalbe Kojak tyre (35-406) construction.

Table 16 illustrates the essential specifications of three types of tyres: Schwalbe Kojak, Michelin 44-406, and Michelin 45-75R16. It is worth noting that the Michelin tyres were specifically engineered for the Shell Eco-Marathon (SEM) competition, with data sourced from [13]. Given that the

Michelin 45-75R16 tyres, with radial construction, are no longer being manufactured, they are utilized as a point of reference for tyres with extremely low resistance. The addition of Michelin 44-406 tyres is intended to assess the potential performance enhancements compared to the currently utilized Schwalbe Kojak tyres.

Table 16 Schwalbe Kojak, Michelin 44-406 and Michelin 45-75R16 tyre data [13]

Tyre	Type	Pressure (bar)	Diameter (mm)	Circumference (mm)	Specified Mass (g)
Schwalbe Kojak 35-406	Bias ply - tubed	4-6.5	494	1552	395
Michelin 44-406	Bias ply – tubed/tubeless	5	496-498	1558-1565	150
Michelin 45-75R16*	Radial ply - tubeless	4-6	466.4	1465	400

**Rolling Resistance Coefficients**

Table 17 Predicted rolling resistance coefficient for each tyre based on tyre loads. illustrates the anticipated rolling resistance figures for individual tyres, calculated using coast-

down test outcomes and the recognized weight distribution of the automobile. Projections for the Michelin 44-406 and 45-75R16 tyres are dependent on inflation pressures of 5 bar and 6 bar, correspondingly.

Table 17 Predicted rolling resistance coefficient for each tyre based on tyre loads.

Wheel	Load (kg)	Tyre	$C_{rr}$	
Front Left	36.2	Schwalbe Kojak	+10%	0.00572
			-	0.00520
			-10%	0.00468
		Michelin 44-406	-	0.00240
		Michelin 45-75R16	-	0.00081
Front Right	36.2	Schwalbe Kojak	+10%	0.00572
			-	0.00520
			-10%	0.00468
		Michelin 44-406	-	0.00240
		Michelin 45-75R16	-	0.00081
Rear	41.9	Schwalbe Kojak	+10%	0.00568

			-	0.00516
			-10%	0.00464
		Michelin 44-406	-	0.00240
		Michelin 45-75R16	-	0.00081

**Michelin Radial 45-75R16**

The Magic Formula, as introduced by Pacejka in 1986, is a well-established empirically grounded mathematical model for tyres [32]. Equation 18 provides a simplified representation of the Magic Formula, which computes cornering stiffness based on inflation pressure and vertical

$$C_{\alpha} = (a_{31} + a_{32}P) \cdot \left( \frac{F_z}{a_{41} + a_{42}P} \right)$$

**Equation 18**

load, specifically for Michelin 45-75R16 radial tyres [33]. The coefficients required for this calculation are detailed in

Table 18. It is important to note that these coefficients are applicable only within defined ranges:  $0.3 < F_z < 0.6 \text{ kN}$  and  $4 < P < 6 \text{ bar}$ .

**Table 18 Cornering stiffness calculation coefficients for Michelin Radial 45-75R16 tyres [33].**

$a_{31}$	$a_{32}$	$a_{41}$	$a_{42}$
<b>57.806</b>	15.101	-0.082	0.186

Figure 26 illustrates the correlation between cornering stiffness and inflation pressure for Michelin 45-75R16 tyres, with data points recorded at 50 N intervals. Up to a load of 450 N, there was a negative association between cornering stiffness and inflation pressure, particularly noticeable at

lower loads. Conversely, for loads surpassing 500 N, there is an opposite correlation, where cornering stiffness rises with increasing inflation pressure. This pattern was highlighted at 600 N, showing a substantial 11.2 N/° increase in cornering stiffness between 4 and 6 bar.

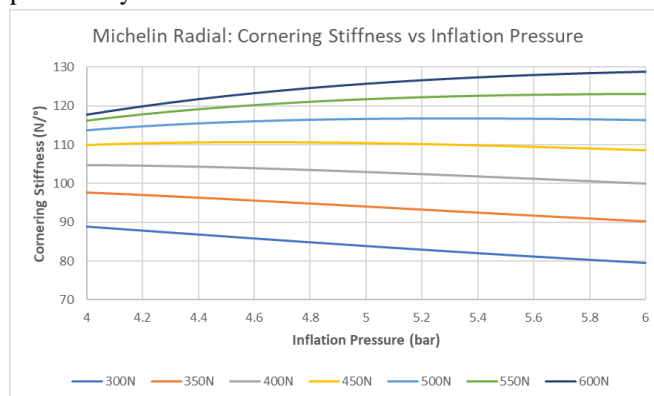


**Figure 26 Michelin 45-75R16 cornering stiffness vs inflation pressure for 300 to 600N of vertical load.**

To guarantee the relevance of the model and mitigate the risk of inaccuracies, adjustments were made to the vertical load exerted on the front axle. It can be observed from

Table 19 that a reduction of 90 N (equivalent to 8.21% of the overall load) was applied.

**Table 19 Utilised and actual front and rear vertical loads.**

	Front Vertical Load ( $F_{zf}$ )	Rear Vertical Load ( $F_{zr}$ )
<b>Actual</b>	690.4N	410.5N
<b>Utilised</b>	600N	410.5N

**Flat Ground**

Figure 27 illustrates the rolling resistance experienced by the tyres, categorised into front left, front right, and rear wheels. For the Schwalbe tires, the front weight distribution resulted in a drag force that was 1.47 N greater on the front tires

compared to the rear tires. This drags disparity further increased to 1.62 N and decreased to 1.326 N under conditions simulating a 10% increase and decrease in  $C_{rr}$ , respectively. In contrast, the Michelin 44-406 and 45-75R16

tyres exhibited significantly lower differential drag forces of 0.67 N and 0.23 N, respectively.

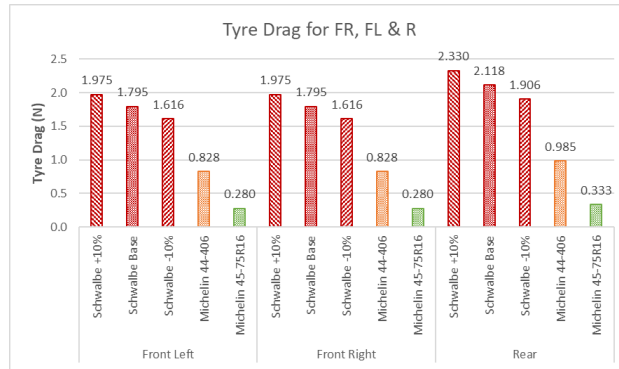


Figure 27 Straight line tyre drag split into wheel location.

Figure 28 presents the predicted tire drag (rolling resistance) for the entire vehicle. The Michelin 45-75R16 tyres demonstrate a significant advantage, with a rolling resistance value below 0.9 N. In contrast, this value escalates dramatically by 534% to 5.7 N for the current Schwalbe tyres.

Notably, utilising the available Michelin 44-406 tyres could potentially reduce straight-line resistance by 53.7%. These findings underscore the critical importance of precise testing, as a seemingly minor 10% increase (0.00052) in  $C_{rr}$  resulted in a substantial rise in drag by 0.571 N.

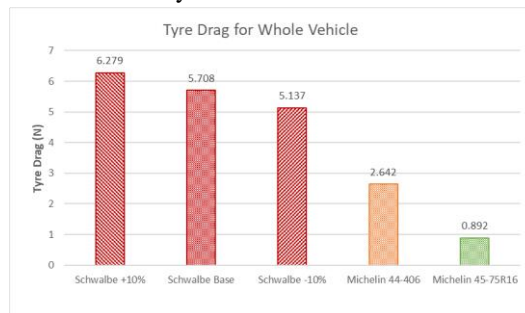


Figure 28 Straight line tyre drag for whole vehicle.

To estimate the total resistive forces acting on the vehicle, aerodynamic properties were predicted, as detailed in

Table 20. In the absence of specific data for the vehicle with wheels, it was projected that the drag coefficient ( $C_d$ ) would increase by up to 40% with the addition of the wheels.

Table 20 Utilised aerodynamic properties.

$C_D$	0.218
$A_F$ (m <sup>2</sup> )	0.3
$\rho$ (kg/m <sup>3</sup> )	1.204

**Sloped Ground**

To quantify the influence of running resistances during an uphill climb, the slope grade was determined using equation as follows, derived from the elevation profile.

$$\theta = \tan^{-1} * (\Delta \text{Elevation} / \Delta \text{Distance}) \tag{Equation 19}$$

Under the assumption of minimal elevation variation between points located 10 meters behind and 6 meters in front of the starting line, the slope gradient over this 16-meter segment was calculated, and the results are presented in

Table 21.

**Table 21 Circuit Paul Armagnac slope gradient at start line.**

Length L (m)	$\Delta$ Elevation (m)	Slope Gradient (°)
16	0.18	0.62

Figure 29 illustrates the climbing resistance plotted against the slope gradient ranging from 0° to 2°, incorporating the rolling resistance characteristics of both the Schwalbe Kojak and Michelin 44-406 tires. This depiction underscores the considerable impact of climbing resistance, even at relatively low slope angles, particularly when considering the constraints imposed by available engine power. Notably, at

the calculated slope gradient of 0.62°, the tractive force necessary to surmount the resistance encountered when moving off the start line amounts to 17.3 N and 14.2 N for the Schwalbe and Michelin tires, respectively. These insights played a pivotal role in informing the design considerations for the gearbox.

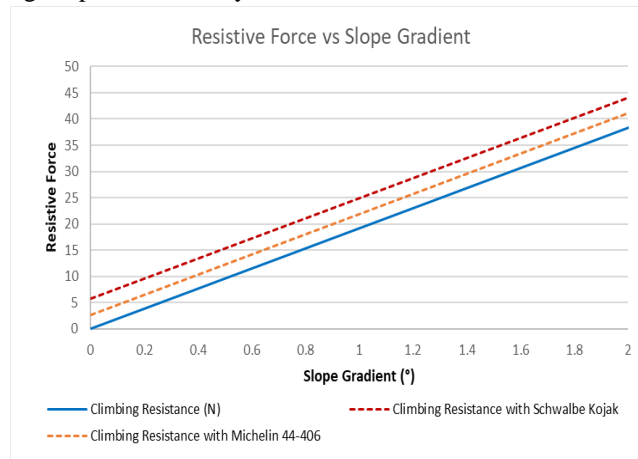


**Figure 29 Resistive force vs slope gradient.**

**Cornering Resistance (Unicycle)**

This section discusses the unicycle model utilised for estimating tire drag, with Figure 30 depicting a free-body diagram of the model. The model operates under the following fundamental assumptions:

- The centre of gravity (CoG) is positioned at the centre of the wheel.

- Slip angle remains within 5° or less.
- Tire response is linear, with a uniform contact patch.
- Cornering conditions are in a steady state.
- The structure is rigid.

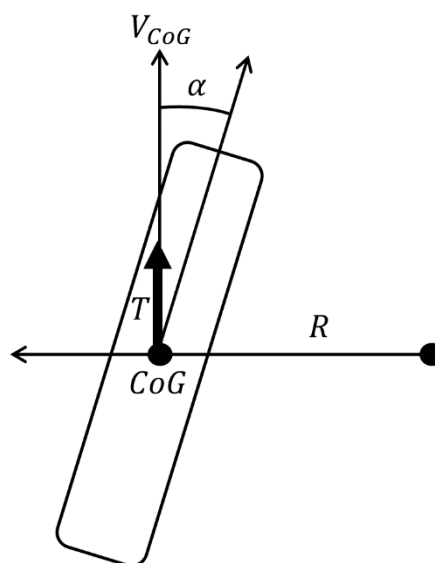


**Figure 30 Simple Unicycle model free-body diagram.**

Expanding upon the foundations of vehicle equilibrium, [33] formulated Equation as follows to calculate the anticipated slip angle.

$$\alpha = \frac{m * \frac{V_{CoG}^2}{R}}{C_{\alpha} - C_{rr} * m * g * \frac{\pi}{180}}$$

Equation 20

After computing the slip angle, the tractive force exerted on the tire was determined utilising following equation. This force corresponds to the tire drag, opposing it to uphold equilibrium.

$$T = C_{\alpha} * \alpha^2 * \frac{\pi}{180} + C_{rr} * m * g$$

Equation 21

**Innovative Design and Solution**

**Arduino control clutch system:**

By utilising a servo motor and an Arduino board, the Arduino-controlled clutch system experienced a noteworthy

enhancement in the operation of the clutch mechanism as shown in Figure 31.

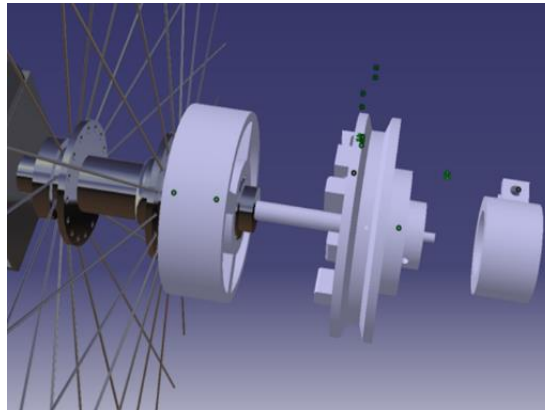


Figure 31 Clutch setup illustration in Catia.

The control of the clutch mechanism by arduino is achieved through the incorporation of a servo motor, which enables precise management of the clutch's engagement and disengagement. This process is facilitated by a straightforward push button located on the steering handle. Power and control for this mechanism are supplied by an Arduino Uno board. One potential obstacle that may arise is the need to stabilize the clutch body. The movement of the clutch is now precisely regulated by a servo motor, resulting in smoother engagement and disengagement triggered by the driver's input via a push button. The implementation of a servo motor and an arduino-based control system has significantly enhanced both the functionality and reliability of the clutch mechanism. To further improve this concept, enhancements to the system and exploration of additional features could be considered to elevate its performance and user satisfaction.

**FEA Calculation and Analysis**

According to the weight restriction established by the team for the SEM project, the rider assumption dictates that the maximum permissible weight is 130 kg. The driver's weight

is approximately 70 kg, representing approximately 53% of the maximum weight limit, thus leaving 60 kg for the entire vehicle, encompassing all internal and external components. In comparison to the optimal cars throughout history, which typically weigh around 26 kg, the average weight of competitor cars falls within the range of 65–85 kg.

To enhance both performance and driver safety, a logical proposition would be to ensure that the weight capacity of the mechanical component is capable of enduring 120% of the maximum weight. This is necessary to allow for a 20% safety margin, indicating that the components should be operational under a load of 156 kg. Consequently, this places the vehicle at the higher end of the typical car weight spectrum, amounting to 86 kg specifically for the car itself.

the force produced by a vehicle in a state of constant velocity is directly related to the size of the impact. While certain components may not bear the full weight of the vehicle, it is crucial to guarantee the resilience of every individual part to endure such forces under extreme circumstances. The calculation of force is presented as follows:

$$Force = Weight = 156 \text{ kg} \times 9.81 \text{ m/s}^2 = 1530.36 \text{ N}$$

Equation 22

When the vehicle is stationary on the ground, it is possible to determine the vertical loads through calculation,  $w_f$  = Weight distribution for front axle,  $w_r$  = Weight distribution for rear axle,  $a$  = Distance from CoG to front axle,  $b$  = Distance from CoG to rear axle and  $L$  = Wheelbase length.

$$w_f = m * g * (a/L)$$

Equation 23

$$w_r = m * g (b/L) \tag{Equation 24}$$

To determine the Centre of Gravity (CoG), it is necessary to utilise the following equations.

$$CoG = \frac{L_{front} * W_{front} + L_{rear} * W_{rear}}{W_{front} + W_{rear}} \tag{Equation 25}$$

$$W_{front} = W_{total} * \text{percentage of total weight on front axle} \tag{Equation 26}$$

The distribution of loads on a chassis structure typically involves various elements, such as crash, ride, static, towing, aerodynamic, cornering, braking, and attractive loads. Analysing the crash scenario poses challenges due to the transition of material properties from elastic to plastic regions, leading to ultimate failure. The ride load holds utmost significance, serving as a key indicator of the vehicle's quality and performance. In the context of the SEM, it is deemed inappropriate to incorporate towing loads in the present analysis. Nonetheless, accounting for aerodynamic, static, and braking loads is essential, given their substantial impact on the structural stress of the chassis. Beyond the direct consequences of different loads, secondary effects like vibrations may arise. Vibrations, characterized by mechanical oscillations occurring in proximity to the equilibrium position, are considered undesirable due to their energy wastage, reduced efficiency, and potential hazards. Machines

exhibit vibrations because of recurring forces and resonance. The primary objective remains the development of a lightweight vehicle at a justifiable cost. Nevertheless, the lightweight nature of components may render them susceptible to vibrations induced by dynamic engine forces, road irregularities, and other external loads. Such susceptibility could, in turn, compromise the safety and stability of the vehicle.

Most significantly, the researchers have identified the utmost braking circumstance as decelerating at a rate of 6 m/s while traveling at velocities ranging from 20 km/h to 30 km/h. This method proves to be a valuable approach in assessing the robustness of the framework and components in enduring such intense braking forces.

The minimum braking force can be calculated by using the maximum weight and the data provided in

Table 22.

$$Force = mass * acceleration = 156 \text{ kg} * \frac{6 \text{ m}}{s^2} = 936 \text{ N} \tag{Equation 27}$$

$$F_{dynamic} (kgf) = \frac{936N}{9.81m/s^2} = 95.41 \text{ kgf} \tag{Equation 28}$$

The calculation of stopping distance can be derived through the application of the subsequent equation:

$$v^2 = u^2 + 2 * a * s \tag{Equation 29}$$

The duration required for complete termination of vehicle motion can be determined utilising the formula provided below:

$$t = \frac{v - u}{a} \tag{Equation 30}$$

Table 22 Braking data.

Maximum Velocity u (m/s)	11.17
Final Velocity v (m/s)	0
Brake Time t (s)	1.86
Braking Distance (m)	10.40
Maximum Deceleration a (m/s <sup>2</sup> )	6
Wheelbase l (mm)	1704.5
Tyre coefficient of friction	0.02

The application of force on the contact area includes more than just the chassis accommodating the driver; the vehicle must also surmount friction, whether it be between components or between the tire and the road. The torque generated by the rotor, along with the overall braking force, are defined as follow.

Where:  $F_{bp}$  (Brake pedal force output),  $F_d$  (Applied brake force),  $P_{cal}$  (Hydraulic pressure to the calliper),  $P_{mc}$  (Hydraulic pressure by the master cylinder),  $A_{mc}$  (Effective area of the master cylinder hydraulic piston),  $A_{cal}$  (Effective area of the calliper hydraulic piston),  $F_{cal}$  (Linear mechanical force by the calliper),  $F_{clamp}$  (Clamp force by the calliper),  $F_{friction}$  (Friction

“Investigation and Design of a Lightweight Three-Wheeled Vehicle for Optimal Fuel Efficiency”

force by the brake pad),  $T_r$  (Torque generated by the rotor),  $T_w$  (Torque in the wheel),  $T_t$  (Torque in the tyre),  $F_{tire}$  (Force in the tyre),  $R_{ef}$  (Effective radius of the rotor),  $R_t$  (Effective

rolling radius of the loaded tire) and  $\mu_{bp}$  (Coefficient of friction between the brake pad and the rotor).

$$F_{bp} = F_d * \{L2/L1\} \tag{Equation 31}$$

$$P_{mc} = F_{bp}/A_{mc} \tag{Equation 32}$$

$$P_{cal} = P_{mc} \tag{Equation 33}$$

$$F_{cal} = P_{cal} * A_{cal} \tag{Equation 34}$$

$$F_{clamp} = 2 * F_{cal} \tag{Equation 35}$$

$$F_{friction} = F_{clamp} * \mu_{bp} \tag{Equation 36}$$

$$T_r = F_{friction} * R_{eff} \tag{Equation 37}$$

$$T_t = T_w = T_r \tag{Equation 38}$$

$$F_{tyre} = T_r/R_t \tag{Equation 39}$$

$$F_{total} = \sum F_{(tyreLF,RF,R)} \tag{Equation 40}$$

Weight distribution data is presented in the Table 23.

**Table 23 Weight distribution data.**

<b>Wheel Radius (mm)</b>	<b>250</b>
<b>Weight on the Front Axle (N)</b>	690.4
<b>Weight on the Rear Axle (N)</b>	410.5
<b>Total Weight (N)</b>	1100.9
<b>Percentage Weight on the Front Axle (%)</b>	62.7
<b>Percentage Weight on the Rear Axle (%)</b>	37.3
<b>Force Applied to Pedal (N)</b>	489
<b>Pedal Ratio</b>	6:01
<b>Force on Balance Bar (N)</b>	2934

The natural frequency plays a pivotal role in the design of structural functional components to avoid the occurrence of resonance. It is essential for the sampling frequency to be a minimum of twice the frequency of the signals under consideration. Consequently, vibration loads should remain

$$[k] - \omega^2 * [M] * \{q\} = 0$$

**CFD Simulation Setup Result and Development**

The CFD simulations were executed using the StarCCM+ software. The initial iteration of the ultimate bodywork design was utilized as the foundation for developing the simulation models. In the preliminary configuration of the CFD simulation, predicated on the guidelines of SEM 2024, the velocity of the vehicle was 11.11 m/s. Optimal meteorological conditions at 20° Celsius and arid atmosphere

within the structural capacity range to guarantee the accuracy of the analysis.

The governing equation for free vibration conditions of a beam is provided as the governing equation that governs the beam and is calculated as follows. Where: k (Stiffness),  $\omega$  (Yaw rate), M (Mass matrix) and q (Degree of freedom).

$$\tag{Equation 41}$$

were additional presumptions applied in the primary setup of the CFD simulation. The dimensions of the wind tunnel in the CFD simulation were established based on the frontal area of the vehicle. The bodywork was positioned 150 mm above the ground as the bodywork prototype was assessed sans wheels to replicate the ground clearance in relation to wheels. A tetra mesh was employed in the CFD simulation, which was arranged during the initial phases of constructing the wind

tunnel. Tetra meshes are smaller than prism layers, and the finer the mesh resolution, the greater the precision of the outcomes, as will be elaborated in the section concerning CFD Results in the project. Two offsets were implemented to enhance the precision of the CFD simulation outcomes. These offsets produce a finer mesh around the vehicle compared to the mesh resolution on the walls of the wind tunnel; hence, the airflow behaviour around the vehicle is precise and can be visually observed with greater clarity.

Upon completion of the CFD simulation, modifications were made to the initial values of the default controls for the automated mesh to ensure mesh independence. Numerous challenges arose during the development of the CFD simulations, with a key issue pertaining to the surface quality of the bodywork. It was noted that cracks were present throughout its surface. This concern was addressed by converting the bodywork into a solid object using CAD

software. Subsequently, skewness angles were identified in the CFD simulation results. The CAD geometry section containing these angles was modified, leading to the emergence of additional skewness angles that were resolved upon reconstructing the entire bodywork model.

Another issue encountered during the simulation involved the  $y+$  geometry, with the error manifesting post-completion and testing of the CFD simulation. Certain sections surrounding the bodywork experienced a collapse in the wall  $y+$  geometry on the mesh. This issue was rectified through remodelling the affected sections.

The computational fluid dynamics (CFD) outcomes pertaining to the initial version of the ultimate bodywork design are analysed through comparison with experimental wind tunnel findings. Figure 32, Figure 33, and Figure 34 illustrate the attained mesh convergence and the outcomes derived from the CFD simulations.

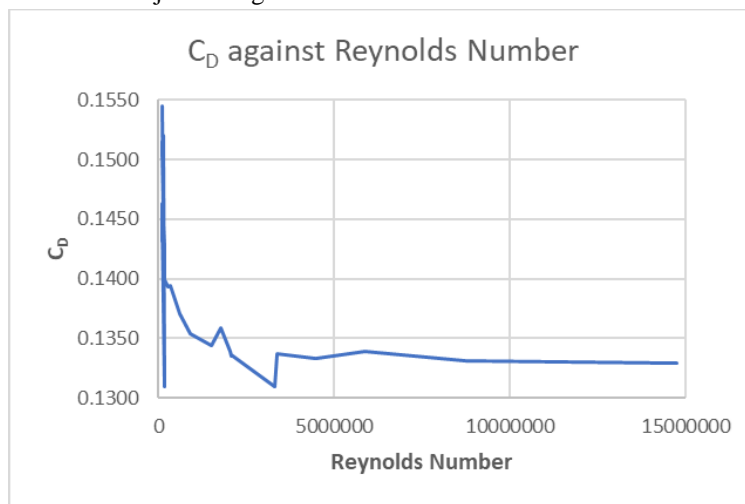


Figure 32  $C_D$  against the Reynolds Number for the initial version of the final bodywork.

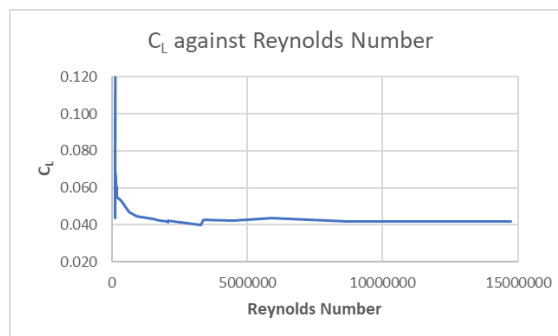


Figure 33  $C_L$  against the Reynolds Number for the initial version of the final bodywork.

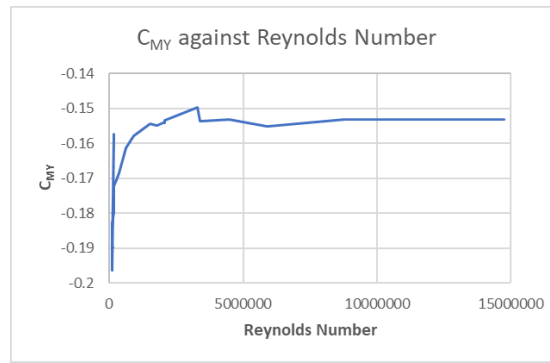


Figure 34  $C_{MY}$  against the Reynolds Number for the first version of the final bodywork.

Mesh convergence was attained upon reaching a cell count of 3,387,514, which was subsequently optimised to achieve the final iteration. The concluding iteration recorded a cell count of 3,295,032, accompanied by a coefficient of drag ( $C_D$ ) of

0.1310, a coefficient of lift ( $C_L$ ) of 0.03999, and a moment coefficient about the yaw axis ( $C_{MY}$ ) of -0.1496. To ensure result accuracy, thirty-five iterations were simulated, with

Table 24 presenting a comprehensive overview of the outcomes from each iteration.

Table 24 The  $C_D$ ,  $C_M$  and  $C_{MY}$  values for each iteration.

Iteration version	Mesh	$C_D$	$C_L$	$C_{MY}$	Changes made for each Iterations
1	104518	0.1545	0.0982	-0.1958	Base settings
2	125693	0.1441	0.0636	-0.1825	Surface curvature 35
3	124623	0.1456	0.0672	-0.1884	Surface curvature 36 volume growth rate 1.8
4	115212	0.1439	0.0682	-0.1882	Volume growth rate 1.6
5	112341	0.1433	0.0678	-0.1934	Volume growth rate 1.5
6	110212	0.1457	0.0659	-0.1882	Volume growth rate 1.4
7	120529	0.1461	0.0712	-0.1900	Core mesh optimisation 0.3
8	112342	0.1453	0.0716	-0.1873	Core mesh optimisation 0.5
9	109778	0.1463	0.0707	-0.1934	Core mesh optimisation 0.8
10	110234	0.1451	0.0724	-0.1965	Core mesh optimisation 0.6
11	184254	0.1310	0.6990	-0.1573	Core mesh optimisation 0.5 volume growth rate 1.1
12	125424	0.1520	0.0435	-0.1927	Core mesh optimisation 0.4 volume growth rate 1.6
13	113460	0.1515	0.0702	-0.1942	Target surface size
14	120345	0.1503	0.0690	-0.1905	Base size 0.2
15	128455	0.1490	0.0690	-0.1898	Target surface size
16	110478	0.1506	0.0701	-0.1903	Target surface size
17	134925	0.1454	0.0640	-0.1814	Target surface size
18	162942	0.1427	0.0610	-0.1798	Core mesh 0.4
19	175936	0.1403	0.0605	-0.1779	Base size 0.19
20	184920	0.1399	0.0550	-0.1723	Base size 0.18
21	286086	0.1393	0.0539	-0.1704	Base size 0.175
22	354529	0.1394	0.0531	-0.1684	Base size 0.15
23	617540	0.1371	0.0472	-0.1614	Base size 0.1
24	911342	0.1354	0.0445	-0.1579	Base size 0.08
25	1512790	0.1344	0.0432	-0.1544	Base size 0.06
26	1780414	0.1359	0.04231	-0.155	Core mesh optimisation 0.5; Volume growth rate 1.5
27	2056191	0.1339	0.04186	-0.1538	Base size 0.05; Core mesh optimisation 0.4
28	2069341	0.1335	0.04158	-0.1542	Core mesh optimisation 0.9

29	2078169	0.1336	0.0421	-0.1533	Base size 0.05
30	3295032	0.1310	0.03999	-0.1496	Volume growth rate 1.1
31	3387514	0.1337	0.0427	-0.1536	Base size 0.04
32	4472400	0.1333	0.0424	-0.1532	Base size 0.035
33	5895685	0.1339	0.0437	-0.1552	Base size 0.03
34	8748071	0.1331	0.04201	-0.1532	Base size 0.025
35	14756735	0.1329	0.04187	-0.1532	Base size 0.02

In Figure 35, a graphical representation illustrates the progression of accumulated drag and lift along the vehicle. The aerodynamic characteristics of the vehicle's design manifest distinct lift dynamics at various sections. Notably, the lift diminishes upon contact with the nose, attributable to the streamlined configuration. Conversely, an augmentation in lift is discerned within the vehicle's midsection, primarily attributed to the angular disposition of the canopy. This

inclination of the canopy generates aerodynamic lift comparable to that of an aerofoil. Furthermore, in the posterior segment of the vehicle, characterised by a widened bodywork angle, the airflow undergoes detachment, thereby contributing to lift generation. These observations underscore the multifaceted interplay between design elements and aerodynamic forces in influencing lift distribution across the vehicle.

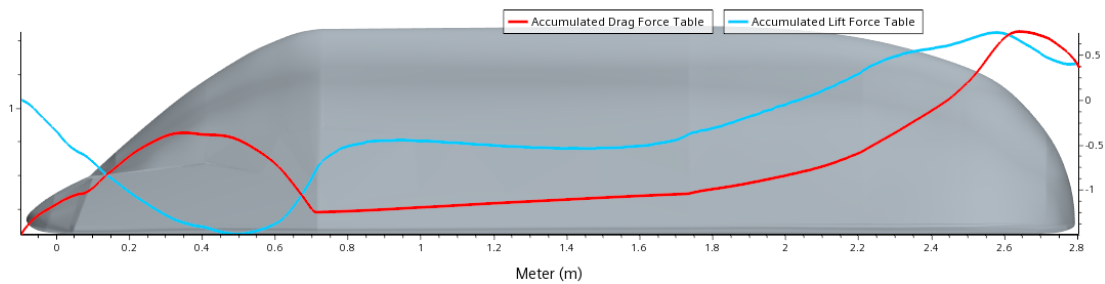


Figure 35 The accumulated CD and CL presented along the length of the vehicle.

It is observed that the drag coefficient experiences a notable increase upon contact with the nose cone, owing to the pronounced steepness characterizing its upper surface design. After the conclusion of the nosecone segment, a stagnation in the drag coefficient is identified, attributed to the cessation of airflow. Along the canopy, a rise in drag coefficient is observed, followed by a subsequent decline, attributable to the geometric configuration of the canopy which induces airflow detachment, thereby facilitating downforce generation. Notably, the rear section of the bodywork exhibits the highest drag coefficient, attributed to the widened angle of the rear segment. A significant detachment of airflow occurs at a vehicle length of 2.9m, coinciding with an observable drop in drag coefficient.

In Figure 36, the Computational Fluid Dynamics (CFD) simulation reveals the wind velocity distribution, highlighting the presence of stagnation zones notably in proximity to the nosecone. Notably, above the nosecone, yellow-coloured regions persist, signifying continued airflow stagnation attributable to the angular relationship between the canopy and the nosecone. A dark red area situated above the canopy signifies air acceleration resulting from detachment. Conversely, in the rear section of the bodywork, stagnation occurs as airflow detaches, consequently leading to a significant decrease in air velocity. Additionally, a wake of low-speed air is observed trailing behind the bodywork, a consequence of the extensive stagnation zones formed on the rear bodywork surface.

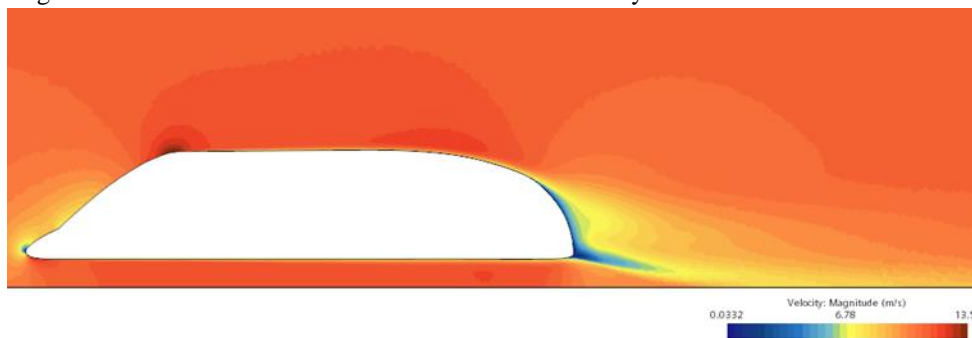


Figure 36 Velocity magnitude behaviour around the bodywork.

The outcomes achieved are deemed acceptable, as the attained coefficient of drag ( $C_D$ ) registers at 1.3, falling below

the predetermined target threshold of 2.0 set forth in the overarching objective for the bodywork. However, a notable

concern arises from the circumstance that this  $C_D$  value of 1.3 was obtained in the absence of attached wheels, posing a limitation as it fails to accurately reflect the performance of the full-scale model.

## RESULTS AND DISCUSSION

The study's findings demonstrated significant advancements in the design and performance of the lightweight three-wheeled vehicle.

Key results are summarized as follows:

### Chassis and Structural Performance:

- The chassis fabricated using 6063-T6 aluminium exhibited a weight reduction of approximately 15% compared to conventional designs while maintaining structural integrity. Finite Element Analysis (FEA) indicated a peak stress of 210 MPa and a deflection of 65 mm under dynamic loading.

### Aerodynamic Analysis:

- Computational Fluid Dynamics (CFD) simulations revealed a drag coefficient ( $C_d$ ) of 0.218, which is a 12% improvement compared to the baseline design. Experimental wind tunnel testing corroborated the simulation results.

### Powertrain Efficiency:

- The modified Honda GX35 engine achieved a brake-specific fuel consumption (BSFC) reduction of 10.15%, improving the vehicle's operational range. Integration of a custom intake and exhaust system further optimized fuel flow and combustion.

### Tire and Rolling Resistance Performance:

- Rolling resistance tests showed a 53.7% reduction when Michelin 44-406 tires were used instead of Schwalbe Kojak tires. The improved tire selection contributed to enhanced overall vehicle efficiency.

### Weight and Distribution:

- The final vehicle weight, including the driver, was measured at 112.22 kg, with a front-heavy weight distribution of 62.7%. This configuration optimized stability and handling characteristics.

The findings of this study underscore the potential of integrating advanced materials and computational methodologies in the design of lightweight vehicles. The implications of these results in the context of existing research are discussed below:

#### 1. Structural and Material Innovations:

- The use of 6063-T6 aluminium aligns with prior research advocating for its weldability and lightweight properties. The observed stress and deflection metrics are consistent with findings by Odi-Owei and Erukainure (2022).

#### 2. Aerodynamic Improvements:

- The achieved drag coefficient ( $C_d$ ) supports existing literature on the benefits of teardrop configurations. The practical implementation of CFD-validated designs marks a

step forward in applying theoretical models to real-world scenarios.

#### 3. Powertrain Optimization:

- The BSFC improvement highlights the efficacy of integrating customized engine components. However, the increased fuel mass input warrants further optimization to balance power output and operational range.

#### 4. Practical and Operational Issues:

- While rolling resistance enhancements through tire selection are notable, further testing under varied road conditions is needed. Additionally, the front-heavy weight distribution may impact handling during rapid manoeuvres, necessitating refinements in suspension and steering design.

#### 5. Study Limitations:

- The study was constrained by the availability of physical testing facilities, limiting the scope of validation. Future work should include real-world testing to verify simulation predictions and expand the applicability of findings.

## CONCLUSIONS

When examining the Shell Eco-Marathon (SEM) project, it is evident that the objectives set for the clutch and drive system were ambitious. The primary aim of the project was to develop a power transmission system that maximised performance through a careful balance of cost, weight, and efficiency, with a focus on ensuring structural integrity and minimising friction. These objectives serve to stimulate innovative approaches towards energy conservation and environmental responsibility.

The paper presents a comprehensive strategy encompassing initial investigations into regulations, evaluation of past designs, enhancement of materials, and a detailed examination of various clutch and transmission systems such as the electromagnetic clutch and Continuously Variable Transmission (CVT). These efforts demonstrate a systematic and analytical decision-making process that facilitates the achievement of set objectives and targets.

Notable advancements have been achieved and opportunities for enhancement include:

- Time Constraints and Revisions

The original intention to utilise a magnetic clutch was substantial but had to be reevaluated due to its complexity and time constraints. Multiple redesigns were necessitated, particularly following the discovery of issues with transmission orientation, significantly prolonging the project timeline. Availability of Materials and Components:

Scarce resources and extended lead times for components posed significant constraints on the project. Consequently, a shift to a more straightforward, practical design incorporating a centrifugal clutch and belt drive was adopted.

- Initial Design Implementation

The aspiration to develop a magnetic clutch was hindered by practical constraints such as limited time and resources. This phase of the project highlights the disparity between

## “Investigation and Design of a Lightweight Three-Wheeled Vehicle for Optimal Fuel Efficiency”

theoretical design and practical execution. Manufacturing Efficiency: Despite encountering challenges, the need for multiple redesigns and deviation from the original concept underscores the potential for enhanced foresight in manufacturing complexity and sourcing materials.

Opting for a centrifugal clutch and belt transmission aligned effectively with the project's objectives given the available time and resources. This decision reflects a sound engineering approach and strategic prioritization of project aims.

- Prospects for Future Endeavours

The report presents a clear roadmap for future initiatives, which may involve comprehensive testing of clutch and transmission performance, further reduction of friction, and a potential revisit to the magnetic clutch concept if feasible. This forward-looking perspective is integral to iterative planning and continual improvement of engineering projects.

- Optimisation of Materials and Design:

Despite limitations, the project successfully identified materials and design elements best suited for the task at hand. Striking a balance between strength and weight while ensuring compatibility with available materials was pivotal in achieving the desired outcome.

Throughout the duration of this project, notable advancements were made in comprehending and applying intricate engineering principles to address a real-world challenge. The principal aim entailed devising a clutch and transmission system that minimized energy consumption, in accordance with the rigorous environmental benchmarks set forth by the Shell Eco-Marathon (SEM). Initially, an ambitious design featuring a magnetic clutch was posited; however, subsequent comprehensive analyses and feasibility evaluations led to the strategic adoption of a more pragmatic centrifugal clutch and belt transmission configuration. This strategic adaptation was instrumental in harmonizing the project's objectives with the overarching goal of optimizing energy efficiency, while concurrently navigating constraints pertaining to temporal, financial, and practical exigencies. While not all initial objectives were attained, the project remained dedicated to achieving optimal energy efficiency within the specified constraints.

While specific subsequent actions are delineated within each section, the fundamental sequential phase in the project entails the fabrication of the conceptual designs. Figure 37, Figure 38, illustrate the master computer-aided design (CAD) representations of the conceptualised vehicle.

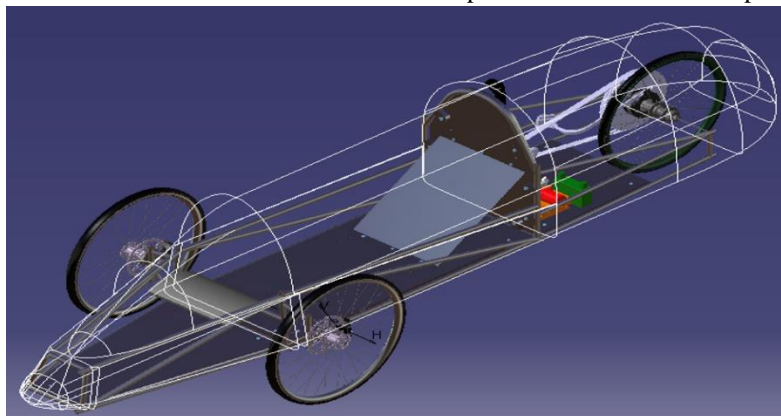


**Figure 37 Master CAD of concept vehicle with no driver.**

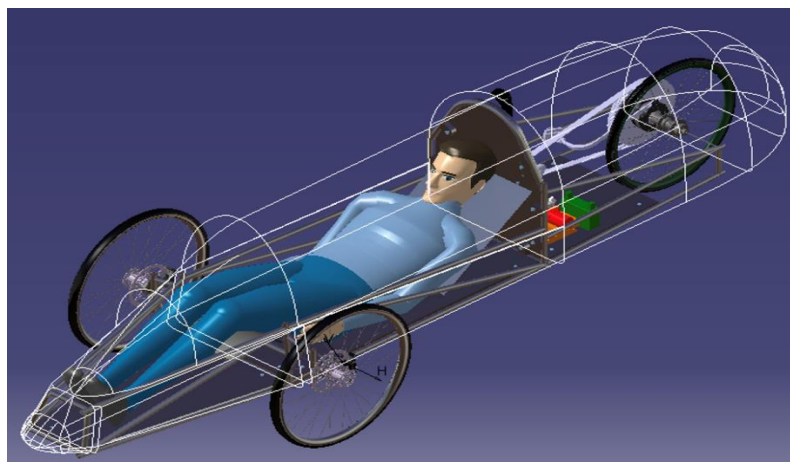


**Figure 38 Master CAD of concept vehicle with driver.**

In conclusion, the objective of the project, focused on the exploration and design of a three-wheeled vehicle with the

primary aim of attaining heightened fuel efficiency via friction mitigation and weight reduction, while concomitantly

adhering to the regulations stipulated by the Shell Eco-Marathon (SEM), has been effectively realised through rigorous investigation, meticulous design processes, and comprehensive modelling endeavours.

**List of abbreviations:**

Some of the symbols listed here have more than one meaning. The context should reveal the precise meaning of the symbol in the document.

<b><u>Symbol</u></b>	<b><u>Description</u></b>
<b>km</b>	Kilometre
<b>kg</b>	Kilogram
<b><math>C_D</math></b>	Drag Coefficient
<b><math>N</math></b>	Newtons
<b>mm</b>	millimetres
<b><math>C_L</math></b>	Lift Coefficient
<b>°</b>	Degrees
<b>%</b>	Percentage
<b>mph</b>	Miles per Hour
<b><math>P</math></b>	Pressure
<b><math>C_{rr}</math></b>	Coefficient of Rolling Resistance
<b><math>F_{rr}</math></b>	Rolling resistance force
<b>cm</b>	Centimetre
<b><math>F_y</math></b>	Lateral force
<b><math>C_\alpha</math></b>	Cornering stiffness
<b><math>\alpha</math></b>	Slip angle
<b>Nm</b>	Newton Metre
<b><math>m/s</math></b>	Metres Per Second
<b><math>F</math></b>	Force
<b><math>m</math></b>	Mass
<b><math>\Delta v</math></b>	Change in Velocity
<b><math>\Delta t</math></b>	Change in Time
<b><math>g</math></b>	Gravitational acceleration
<b><math>m</math></b>	Metres
<b><math>C_{MY}</math></b>	Pitch Moment
<b><math>C_{DA}</math></b>	Area Drag Coefficient
<b><math>F_D</math></b>	Aerodynamic Drag Force
<b><math>\rho</math></b>	Density
<b><math>v</math></b>	Velocity
<b><math>A</math></b>	Reference Area
<b><math>F_L</math></b>	Aerodynamic Lift Force
<b><math>Re</math></b>	Reynolds number
<b><math>L</math></b>	Length
<b><math>\mu</math></b>	Dynamic viscosity
<b><math>\mu m</math></b>	Micrometres
<b><math>g</math></b>	Grams
<b><math>kW</math></b>	Kilowatt
<b>K</b>	Kelvin
<b><math>w_f</math></b>	Front weight distribution
<b><math>w_r</math></b>	Rear weight distribution
<b><math>a</math></b>	X distance from CoG to front axle
<b><math>b</math></b>	X distance from CoG to rear axle
<b><math>s</math></b>	Distance
<b><math>u</math></b>	Initial velocity
<b><math>a</math></b>	Acceleration
<b><math>t</math></b>	Time
<b><math>F_{bp}</math></b>	Brake pedal force output
<b><math>F_d</math></b>	Applied brake force

“Investigation and Design of a Lightweight Three-Wheeled Vehicle for Optimal Fuel Efficiency”

$L1$	Distance from the brake pedal arm pivot to the output rod clevis attachment
$L2$	Distance from the brake pedal arm pivot to the brake pedal pad
$P_{mc}$	Hydraulic pressure by the master cylinder
$A_{mc}$	Effective area of the master cylinder hydraulic piston
$P_{cal}$	Hydraulic pressure to the calliper
$F_{cal}$	Linear mechanical force by the calliper
$A_{cal}$	Effective area of the calliper hydraulic piston
$F_{clamp}$	Clamp force by the calliper
$F_{friction}$	Frictional force by the brake pads
$\mu_{bp}$	Coefficient of friction between the brake pad and the rotor
$T_r$	Torque generated by the rotor
$R_{eff}$	Effective radius of the rotor
$T_t$	Torque in the tyre
$T_w$	Torque in the wheel
$F_{tyre}$	Force in the tyre
$R_t$	Effective rolling radius of the loaded tire
$k$	Stiffness Matrix
$q$	Degree of freedom
$M$	Mass matrix
$^{\circ}C$	Degrees Celsius
$J$	Joules
$F_{Rtotal}$	Total Resistive force
$F_{mech}$	Mechanical resistive force
$F_z$	Vertical load
$F_{zf}$	Front Vertical load
$F_{zr}$	Rear Vertical load
$F_{St}$	Climbing resistance
$\theta$	Gradient slop angle
$V_{CoG}$	Velocity at centre of gravity
$R$	Radius
$T$	Tractive Force
$F_{yf}$	Lateral force at front axel
$F_{yr}$	Lateral force at rear axel
$C_{af}$	Front cornering stiffness
$C_{ar}$	Rear cornering stiffness
$\alpha_f$	Front slip angle
$\alpha_r$	Rear slip angle
$M_z$	Yaw moment
$I_{zz}$	Yaw moment of inertia
$m_f$	Mass on front axle
$m_r$	Mass on rear axle
$\dot{\omega}_z$	Yaw acceleration
$\omega_z$	Yaw rate
$\dot{V}_y$	Lateral acceleration
$V_y$	Lateral velocity
$\delta$	Steered angle at wheels

**Abbreviations**

**Description**

<b>1D</b>	One Dimensional
<b>2D</b>	2 Dimensional
<b>3D</b>	3 Dimensional

<b>BDC</b>	Bottom Dead Centre
<b>BMEP</b>	Brake Mean Effective Pressure
<b>BSFC</b>	Brake Specific Fuel Consumption
<b>CO<sub>2</sub></b>	Carbon Dioxide
<b>CO</b>	Carbon Monoxide
<b>CoG</b>	Centre of Gravity
<b>CR</b>	Compression Ratio
<b>CFD</b>	Computational Fluid Dynamics
<b>CAD</b>	Computer Aided Design
<b>CVT</b>	Continuously Variable Transmission
<b>ECU</b>	Engine Control Unit
<b>FEA</b>	Finite Element Analysis
<b>FS</b>	Formula Student
<b>ICE</b>	Internal Combustion Engine
<b>MDF</b>	Medium-Density Fibreboard
<b>MIG</b>	Metal Inert Gas
<b>NO<sub>x</sub></b>	Nitrogen Oxides
<b>PLA</b>	Polylactic Acid
<b>PSI</b>	Pounds per Square Inch
<b>RPM</b>	Revolutions per Minute
<b>SEM</b>	Shell Eco-Marathon
<b>T</b>	Tempered alloy series
<b>TDC</b>	Top Dead Centre
<b>TIG</b>	Tungsten Inert Gas
<b>VD</b>	Vehicle Dynamics

## DECLARATIONS

**Availability of data and materials:** Data and materials are available upon reasonable request.

**Competing interests:** The authors declare no conflicts of interest.

**Funding:** The authors declare no specific funding was received for this study.

**Authors' contributions:**

**KH major contribution:** conceptualization; methodology; supervision; data curation; writing—original draft preparation; writing—review and editing, **GW major**

**contribution:** conceptualization; methodology; visualization; supervision; project administration; resources,

**LN major contribution:** methodology; software; validation; formal analysis; investigation. All authors read and approved the final manuscript.

**Acknowledgments:** The authors express gratitude to Coventry University for their support and resources.

## REFERENCES

1. H. Ahmad, A. A. Markina, M. V. Porotnikov, and F. Ahmad, ‘A review of carbon fiber materials in automotive industry’, in *IOP Conference Series: Materials Science and Engineering*, IOP Publishing Ltd, Nov. 2020. doi:10.1088/1757-899X/971/3/032011.
2. S. Odi-Owei and F. E. Erukainure, ‘The design process of the chassis of a prototype vehicle for Shell Eco-marathon’, 2022, doi: 10.21203/rs.3.rs-1402102/v2.
3. E. Tsirogiannis, G. Siasos, G. Stavroulakis, and S. Makridis, ‘Lightweight Design and Welding Manufacturing of a Hydrogen Fuel Cell Powered Car’s Chassis’, *Challenges*, vol. 9, no. 1, p. 25, May 2018, doi: 10.3390/challe9010025.
4. E. Tsirogiannis, G. Siasos, G. Stavroulakis, and S. Makridis, ‘Lightweight Design and Welding Manufacturing of a Hydrogen Fuel Cell Powered Car’s Chassis’, *Challenges*, vol. 9, no. 1, p. 25, May 2018, doi: 10.3390/challe9010025.
5. E. Kozák, Á. Gégény, F. Zombori, S. Forrai, and I. Péter Szabó, ‘Eco-marathon racing car casing and frame structure design’, *IOP Conf Ser Mater Sci Eng*, vol. 1237, no. 1, p. 012010, May 2022, doi: 10.1088/1757-899X/1237/1/012010.
6. A. Messana *et al.*, ‘From design to manufacture of a carbon fiber monocoque for a three-wheeler vehicle prototype’, *Materials*, vol. 12, no. 3, Jan. 2019, doi: 10.3390/ma12030332.
7. D. Rogiest, V. Colomer-Romero, J. I. Martinez Sanchez, and A. V Martinez-Sanz, ‘Design of a Fuel-Efficient Prototype’s Monocoque’, 2011, doi: 10.13140/RG.2.1.2364.8725.

8. P. Kah, H. Väst, P. Kah, E. Hiltunen, and J. Martikainen, ‘Investigation of Hot Cracking in the Welding of Aluminium Alloys (6005 & 6082)’, 2010, doi: 10.13140/2.1.4215.6324.
9. S. Cui, Y. Yu, R. Ma, F. Tian, and S. Pang, ‘Study on Morphology, Microstructure and Properties of 6063-T6 Aluminum Alloy Joints in MIG Welding’, *Materials*, vol. 16, no. 13, Jul. 2023, doi: 10.3390/ma16134886.
10. M. Lucic and M. Lučić, ‘Structural analysis of Formula Student vehicle chassis using Ansys software’, 2023. [Online]. Available: <https://www.researchgate.net/publication/369416494>
11. E. Abo-Serie, E. Oran, and O. Utcu, ‘AERODYNAMICS ASSESSMENT USING CFD FOR A LOW DRAG SHELL ECO-MARATHON CAR’, Yildiz Technical University Press, 2017.
12. M. Fabian, M. Puškár, R. Boslai, M. Kopas, Š. Kender, and R. Huňady, ‘Design of experimental vehicle specified for competition Shell Eco-marathon 2017 according to principles of car body digitisation based on views in 2D using the intuitive tool Imagine&Shape CATIA V5’, *Advances in Engineering Software*, vol. 115, pp. 413–428, Jan. 2018, doi: 10.1016/j.advengsoft.2017.10.006.
13. J. J. (Jean J. Santin, *The world’s most fuel efficient vehicle : design and development of PAC-Car II*. Vdf Hochschulverlag AG an der ETH Zürich, 2007.
14. E. Kozák, Á. Gégény, F. Zombori, S. Forrai, and I. Péter Szabó, ‘Eco-marathon racing car casing and frame structure design’, *IOP Conf Ser Mater Sci Eng*, vol. 1237, no. 1, p. 012010, May 2022, doi: 10.1088/1757-899x/1237/1/012010.
15. A. M. Ail Ganesan and P. Darul Ridzuan, ‘Design and Development of Body Panel for UTP’s Shell Eco-Marathon Vehicle by’, 2011.
16. F. Arpino, G. Cortellessa, A. Frattolillo, F. Iannetta, and M. Scungio, ‘Numerical and experimental investigation of the flow over a car prototype for the Shell Eco Marathon’, *Journal of Applied Fluid Mechanics*, vol. 12, no. 1, pp. 207–218, 2019, doi: 10.29252/jafm.75.253.28884.
17. O. Pires, X. Munduate, K. Boorsma, O. Ceyhan Yilmaz, H. Aa Madsen, and W. A. Timmer, ‘Experimental investigation of Surface Roughness effects and Transition on Wind Turbine performance’, in *Journal of Physics: Conference Series*, Institute of Physics Publishing, Jun. 2018. doi: 10.1088/1742-6596/1037/5/052018.
18. K. S. Umesh, V. K. Pravin, and & K. Rajagopal, ‘CFD ANALYSIS OF EXHAUST MANIFOLD OF MULTI-CYLINDER SI ENGINE TO DETERMINE OPTIMAL GEOMETRY FOR REDUCING EMISSIONS’, 2013.
19. D. Di Battista, M. Di Bartolomeo, and R. Cipollone, ‘Flow and thermal management of engine intake air for fuel and emissions saving’, *Energy Convers Manag*, vol. 173, pp. 46–55, Oct. 2018, doi: 10.1016/j.enconman.2018.07.074.
20. J. Li, C. M. Gong, Y. Su, H. L. Dou, and X. J. Liu, ‘Effect of injection and ignition timings on performance and emissions from a spark-ignition engine fueled with methanol’, *Fuel*, vol. 89, no. 12, pp. 3919–3925, Dec. 2010, doi: 10.1016/j.fuel.2010.06.038.
21. R. C. Costa and J. R. Sodré, ‘Compression ratio effects on an ethanol/gasoline fuelled engine performance’, *Appl Therm Eng*, vol. 31, no. 2–3, pp. 278–283, Feb. 2011, doi: 10.1016/j.applthermaleng.2010.09.007.
22. J. Benajes, R. Novella, J. Gomez-Soriano, P. J. Martinez-Hernandez, C. Libert, and M. Dabiri, ‘Evaluation of the passive pre-chamber ignition concept for future high compression ratio turbocharged spark-ignition engines’, *Appl Energy*, vol. 248, pp. 576–588, Aug. 2019, doi: 10.1016/j.apenergy.2019.04.131.
23. L. Ydrefors, M. Hjort, S. Kharrazi, J. Jerrelind, and A. Stensson Trigell, ‘Rolling resistance and its relation to operating conditions: A literature review’, *Proceedings of the Institution of Mechanical Engineers, Part D: Journal of Automobile Engineering*, vol. 235, no. 12, pp. 2931–2948, Oct. 2021, doi: 10.1177/09544070211011089.
24. W. Gołębiewski, ‘IMPACT OF OUTER DIAMETER AND ENERGY EFFICIENCY CLASS OF TYRE ON FUEL CONSUMPTION OF A PASSENGER CAR AT CONSTANT VELOCITY’, *Journal of KONES. Powertrain and Transport*, vol. 22, no. 2, pp. 71–78, Jan. 2015, doi: 10.5604/12314005.1165664.
25. M. Djordjevic, A. Jankovic, and B. Jeremic, ‘Rolling resistance as the risk factor for fuel consumption’, *International Journal of Vehicle Systems Modelling and Testing*, vol. 4, no. 3, pp. 185–200, 2009, doi: 10.1504/IJVSMT.2009.029388.
26. E. HOSOBUCHI, C. MISAKI, N. KATAYAMA, and K. DOWAKI, ‘Impact of Increased Tire Pressure on Fuel Consumption and Environment for Fuel-Cell-Assisted Shared Bicycles’, 2021.
27. D. Gunev and S. Iliev, ‘The basic geometric parameters of the driving position of a battery electric, prototype class vehicle for the Shell Eco-marathon competition’, in *AIP Conference Proceedings*, American Institute of Physics Inc., Oct. 2021. doi: 10.1063/5.0069048.
28. C. Cravero and D. Marsano, ‘Computational Investigation of the Aerodynamics of a Wheel

Installed on a Race Car with a Multi-Element Front Wing’, *Fluids*, vol. 7, no. 6, Jun. 2022, doi: 10.3390/fluids7060182.

29. E. S. Aziz, C. Chassapis, S. Esche, S. Dai, S. Xu, and R. Jia, ‘Online wind tunnel laboratory’, in *ASEE Annual Conference and Exposition, Conference Proceedings*, American Society for Engineering Education, 2008. doi: 10.18260/1-2--3402.
30. H. Taghavifar and A. Mardani, ‘Investigating the effect of velocity, inflation pressure, and vertical load on rolling resistance of a radial ply tire’, *J Terramech*, vol. 50, no. 2, pp. 99–106, 2013, doi: 10.1016/j.jterra.2013.01.005.
31. F. Synák and A. Kalašová, ‘Assessing the Impact of the Change in the Tire Pressure on the Rolling Resistance and Fuel Consumption’, *Advances in Science and Technology Research Journal*, vol. 14, no. 3, pp. 100–106, Sep. 2020, doi: 10.12913/22998624/120801.
32. Blundell: M and Harty; D, *Multibody Systems Approach to Vehicle Dynamics*. 2015.A
33. J.-J. Santin *et al.*, *The World’s Most Fuel Efficient Vehicle*. vdf Hochschulverlag AG an der ETH Zürich, 2007. doi: 10.3218/4139-2.